The Sensitivity of Tidal Channel Systems to Initial Bed Conditions, Vegetation, and Tidal Asymmetry

L. Geng[1,2,3], S. Lanzoni[2], A. D'Alpaos[4], A. Sgarabotto[2], and Z. Gong[1*]

[1]State Key Laboratory of Hydrology Water Resources and Hydraulic Engineering, Hohai University, Nanjing, China.

[2]Department of Civil, Environmental and Architectural Engineering, University of Padova, Padua, Italy

[3]State Key Laboratory of Estuarine and Coastal Research, East China Normal University, Shanghai, China

[4]Department of Geosciences, University of Padova, Padua, Italy.

Corresponding author: Zheng Gong (gongzheng@hhu.edu.cn)

Key Points:

- Randomly-distributed bed perturbation may increases channel drainage efficiency by changing the channel network structure.
- Vegetation promotes channel elongation and drainage efficiency, while a sloping basin has opposite effects due to reduced tidal prism.
- Ebb-dominant conditions produce a rearrangement of total channel length and mean unchanneled length, ensuring a higher drainage efficiency.

Abstract

In tidal environments, channel networks act as essential drainage pathways. Although the complex interactions between environmental factors have been studied extensively, the effects of the initial bathymetry on tidal network ontogeny are poorly understood. In this contribution, we used a numerical model to mimic a schematic tidal basin subjected to tidal forcing. The effects of the initial bathymetry and vegetation growth are analyzed by changing the features of randomly-generated bed perturbation and the intertidal platform slope. Different perturbation densities mildly affect the growth of tidal networks, which, at equilibrium, share similar values in terms of channel length, tidal prism, and cross-sectional area. The complexity and structure of channel networks are more sensitive to variations in perturbation distribution. Increasing the initial bathymetry slope can shorten channels and reduce the tidal prism and drainage efficiency. Vegetation growth is found to invariably promote channel lengthening and narrowing, increasing the complexity and drainage efficiency of the system. An asymmetrical tidal forcing generally leads to longer channels and smaller unchanneled lengths. Under ebb-dominant conditions, channels get deeper, and the increased channel length ensures a higher drainage efficiency. Insights of our study provide a deeper understanding of the environmental factors controlling the equilibrium morphology of tidal channel systems and their overall resilience. Further implications concern the restoration and management of coastal areas through the informed use of topographic manipulation and planting arrangement. Finally, accounting for the uncertainties associated with initial conditions is relevant when modeling other earth systems and comparing them with real systems.

Plain Language Summary

Tidal channels in coastal landscapes connect the sea and the inner land, acting as essential drainage pathways for exchanging water, sediments, and nutrients. The channel network morphology and drainage efficiency exhibit different sensitivities to environmental factors. In this study, a tide-dominated intertidal basin is simulated through a numerical program to analyze the tidal channel characteristics influenced by initial bed topography, vegetation, and enhanced flood- or ebb-currents. Randomly-distributed bed perturbation can significantly change the channel network structure, leading to more complex channel networks with more channel branches. The presence of vegetation generally provides a dramatic increase in channel expansion and drainage efficiency. However, the positive effect of vegetation on channel drainage efficiency may be weakened with the increase of bed slope. Furthermore, under ebb-dominant conditions, the tidal channel system will dissect the tidal basin more efficiently, resulting in a higher drainage efficiency than in flood-dominant conditions. These findings are relevant for assessing the resilience of tidal channel systems and could be useful for the design of restoration projects and the management of coastal areas.

1 Introduction

Tidal networks stem from the complex interactions between hydrodynamics, sediment transport, and biotic processes (Fagherazzi & Sun, 2004; D'Alpaos et al., 2007; Vlaswinkel & Cantelli, 2011; Coco et al., 2013; D'Alpaos and Marani, 2016; Kearney & Fagherazzi, 2016). These mutual interactions drive the evolution of tidal environments and under constant forcing conditions, determine the equilibrium configuration of tidal channels, tidal flats, and salt marshes. Even though tidal networks have been broadly investigated, assessing the impact of the initial bathymetry on the growth of tidal networks remains understudied. Similarly, addressing

the role of the tidal forcing is crucial for evaluating how a net import/export of sediment can ultimately alter tidal channel features.

The morphology of an intertidal platform can be characterized, on small spatial scales, by perturbations of the bed surface with respect to a plane configuration and, on a larger scale, by the platform slope. Small-scale bed perturbations are quite common in the field, and can vary significantly in shape and size (e.g., Figure 1). They are widely used in numerical models to accelerate the geomorphological evolution and obtain realistic tidal channel features (D'Alpaos et al., 2005; Van der Wegen et al., 2008; Belliard et al., 2015; Xu et al., 2017). In laboratory experiments, the initial bathymetry has bed irregularities, whose height and distribution depend on the methodology used to prepare and screed the initial sediment bed (Stefanon et al., 2010; Iwasaki et al., 2013; Kleinhans et al., 2014; Geng et al., 2020). In general, bed unevenness influences local patterns of erosion and deposition (Hancock et al., 2016). When propagating on the intertidal platform, tidal currents become more intense in deeper areas, leading to higher bottom shear stresses and erosion rates (D'Alpaos et al., 2005; Stefanon et al., 2010; Coco et al., 2013) and, hence, favoring channel initiation (Iwasaki et al., 2013; Kleinhans et al., 2014).

A highly perturbed bed surface may increase the density and complexity of tidal channel networks (Belliard et al., 2015) and induce substantial changes in evolutionary trajectories, eventually leading to different equilibrium states, evolution hysteresis, or rapid topography changes (Perron & Fagherazzi, 2012; Zhang et al., 2018). In both numerical and physical models, changing the distribution of initial bed perturbations can lead to different channel network structures (Stefanon et al., 2010; Zhou & Olabarrieta et al., 2014; Zhou & Stefanon et al., 2014). Moreover, the raised soil surface of bed irregularities can favor the formation of vegetation patches (Figure 1), due to the shorter inundation period (Mudd et al., 2004; Kirwan et al., 2010; Hu et al., 2015) and the enhanced sediment oxygenation (Fivash et al., 2020; Mossman et al., 2020). The presence of these patches enhances spatial variations on bed roughness, which further affect channel development and, ultimately, the network structure (Temmerman et al., 2007; Kirwan et al., 2014; D'Alpaos & Marani, 2016). The flow concentration between vegetation patches, in fact, promotes channel initiation (Vandenbruwaene et al., 2011; Temmerman et al., 2012; Van Oyen et al., 2014) and, in general, increases the drainage efficiency of tidal channel networks (Temmerman et al., 2007; Kearney & Fagherazzi, 2016).

On a large scale, a relevant morphological feature of a tidal basin is the longitudinal bed slope (Yapp et al., 1916 & 1917; Beeftink, 1966). Extensive mudflats with a sloping profile typically form along deposition-dominated open coasts (e.g., the Jiangsu Coast, China) subject to a sufficient external sediment supply (Bearman et al., 2010; Gong et al., 2017). The mudflat slope can increase in the presence of a large tidal amplitude because of the erosion in lower intertidal areas (Roberts et al., 2000; Pritchard et al., 2002). In this type of environment, no explicit quantitative relation has been found to estimate the size and scale of tidal channels. Conversely, in sheltered tidal basins characterized by a net loss of sediment, like the Venice Lagoon (Tambroni & Seminara, 2006; Defina et al., 2007; Carniello et al., 2012; Tognin et al., 2021), the tidal flats remain nearly horizontal (Carniello et al., 2009; Tommasini et al., 2019; Roner et al., 2021). Tidal channels draining these flats have been found to have cross sections that follow the classic tidal-prism channel-area $(P - A)$ relationship (O'Brien, 1969; Jarrett, 1976; Hughes, 2002; D'Alpaos et al., 2010). This relationship relates the channel area to the tidal prism through a power-law relationship and has been widely employed to describe the equilibrium cross sections of tidal inlets and sheltered channels.

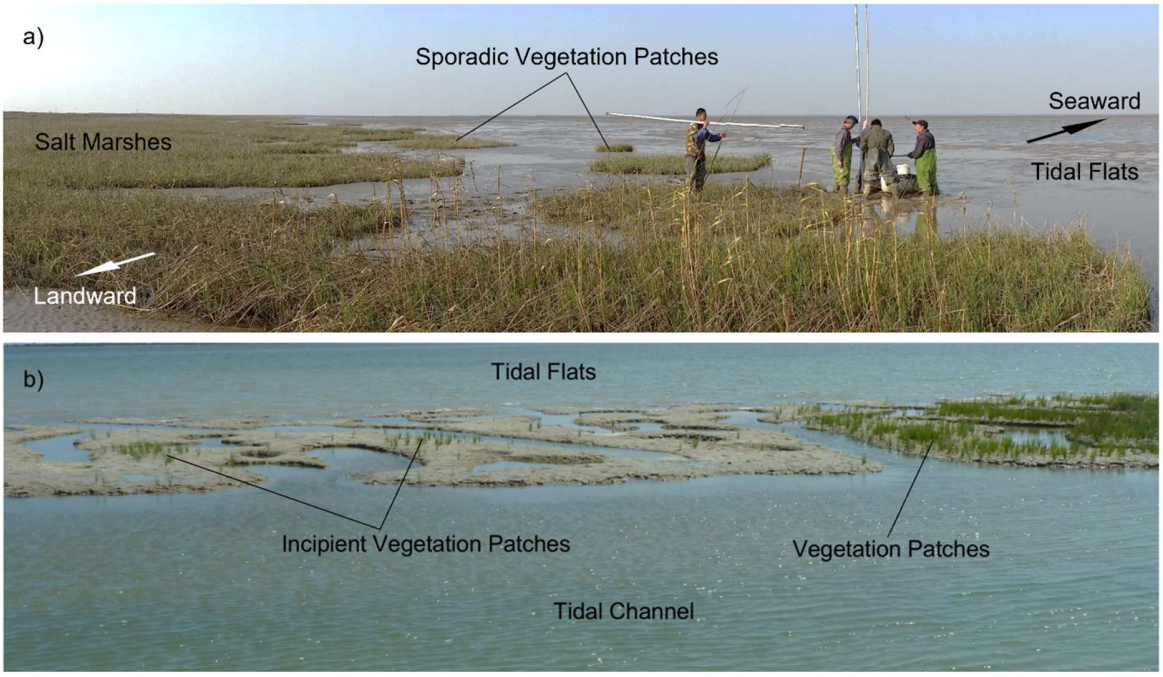

Figure 1. Example of vegetation patches observed (**a**) along the Jiangsu Coast (China), characterized by a sloping bathymetry, and (**b**) on the almost horizontal tidal flats bordering a tidal channel in the Venice Lagoon (Italy).

The development of salt marshes, in general, depends on the steepness and elevation of the tidal flats colonized by vegetation (Pennings & Callaway, 1992). In Jiangsu Coast (China), *Spartina* starts to grow on the higher mudflat areas (Figure 1a), and, hence, salt marshes progressively expand seaward (Zhang et al., 2004; Li et al., 2018). A seaward salt marsh expansion has been observed in other coastal areas worldwide, such as in the Westerschelde Estuary (Zuidgors and Waarde marshes, SW Netherlands; Cox et al., 2003), and in the Tagus Estuary (Pancas marshes, Portugal; Lopes et al., 2020). In these tidal settings, owing to the significant difference in deposition rates between salt marshes and tidal flats, a steep cliff may occur at the marsh edge (Cox et al., 2003; Fagherazzi et al., 2012). On the other hand, in sheltered tidal basins with a limited or nearly absent external supply of sediment as the Venice Lagoon, salt marshes often develop near the border of tidal channels (Figure 1b), where the sediment needed to build the marsh may accumulate (Tambroni & Seminara, 2006; Defina et al., 2007; Carniello et al., 2012). The salt marshes then gradually extend further away from the channel border, and new creeks form in the vegetated areas driven by headward erosion (Fagherazzi & Sun, 2004; D'Alpaos et al., 2005; Hughes et al., 2009). It thus clearly appears that salt marshes formed in weakly or strongly sloping tidal settings exhibit different temporal and spatial evolution. In turn, the initial bed topography affects the overall tidal channel development and the drainage efficiency at equilibrium.

In most modeling studies addressing the morphodynamics of tidal networks, the motion is forced by a semidiurnal tidal constituent (e.g., M2 and S2) imposed at the sea boundary (D'Alpaos et al., 2007; Coco et al., 2013; Belliard et al., 2015). Overtides, and the corresponding advective sediment fluxes, are thus generated only within the tidal basin. Nevertheless, the net import/export of sediment due to externally prescribed overtides (e.g., M4 and S4) may affect the

final equilibrium morphology (Ter Brake & Schuttelaars, 2010; Meerman et al., 2019), depending on the relative amplitude of overtides with respect to the principal tidal constituent (Toffolon & Lanzoni, 2010).

This contribution analyzes the coupled evolution of tidal channels and salt marshes under different initial bed configurations for a tidal forcing containing either a single semidiurnal tidal constituent (S2) or also a combination of overtides (S4 and S6) leading to an ebb-dominant or flood-dominant forcing. The specific research questions we intend to answer are: (1) What is the effect of initial bed perturbations on tidal channel and salt marsh patterns? (2) How does the initial slope of the intertidal platform affect the growth and interaction of channel networks and salt marshes? (3) What are the effects of overtides on the evolution of tidal channels? (4) Which are the critical factors favoring the drainage efficiency of tidal networks? Answers to these questions will help to further unravel the eco-morphodynamics of tidal channel networks and their equilibrium morphologies.

2 Materials and Methods

This study focuses on the effects that initial irregularities of the bed surface and the growth of vegetation may have on the evolution and the final morphology of tidal channels forming in the schematic tidal basin shown in Figure 2. The basin is 400 m wide and 500 m long, and it is connected seaward to a large channel or an open coast. There, we impose either a semidiurnal tide with a given amplitude or a tide with three main constituents, reproducing ebb-dominant or flood-dominant conditions. Moreover, at the seaward border, we prescribe the sediment concentration, mimicking the sediment input supplied externally to the basin. The initial basin configuration consists of a randomly-perturbed initial bathymetry either flat or tilted with a prescribed seaward slope. The subsequent eco-morphodynamic evolution is computed by means of the process-based model developed in Geng et al. (2021).

Below, we briefly recall the main characteristics of the four modules constituting the eco-morphodynamic model, referring the reader to Geng et al. (2021) for the details. We then describe how the numerical simulations have been designed in order to unravel the legacy of initial bathymetry and tidal forcing on the morphology of the tidal networks which eventually form in the basin.

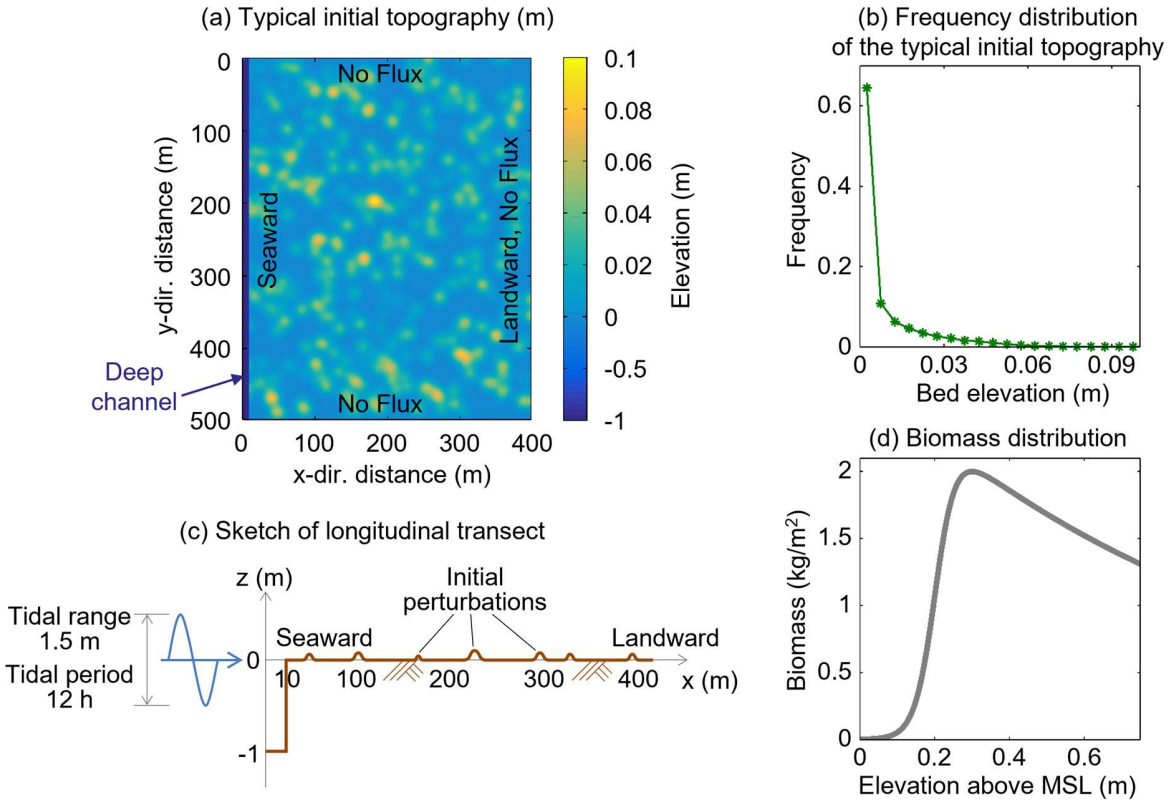

Figure 2. The setup of the simulated tidal basin: (a) Top view of the initial basin topography and of the imposed boundary conditions. (b) Frequency distribution of the perturbation patches characterizing the initial bed topography. (c) Sketch of a typical initial longitudinal transect. (d) Biomass distribution used to model vegetation dynamics in this study.

2.1 The eco-morphodynamic model

The interactions between the morphological units (tidal channels, tidal flats, and salt marshes) composing the tidal basin are simulated by an eco-morphodynamic model describing the hydrodynamics, suspended sediment transport, bed evolution, and vegetation dynamics.

The tidal basin is assumed to be dominated by the tidal forcing and, hence, wind effects and river inflow are neglected as a first approximation. Friction is assumed to prevail over inertia owing to the small flow depth D occurring in the tidal basin. As a consequence, friction balances the gravitational action associated with the free surface slope in the momentum equations (Rinaldo et al., 1999; D'Alpaos et al., 2007). Wetting and drying processes are treated as in Defina (2000). With the above approximations, the components of the depth-averaged velocity in the longitudinal (x) and lateral (y) directions read:

$$U_x = \frac{-K_s^2}{\sqrt{{U_x}^2+{U_y}^2}}\left(\frac{\phi}{D}\right)^2 \frac{\partial \zeta}{\partial x} \quad (1)$$

$$U_y = \frac{-K_s^2}{\sqrt{{U_x}^2+{U_y}^2}}\left(\frac{\phi}{D}\right)^2 \frac{\partial \zeta}{\partial y} \quad (2)$$

while, at each instant t of the tidal cycle, the variations of the water level $\zeta(x, y, t)$, referred to the instantaneous value of the sea level at the seaward border $\xi(t)$, are described by the equation (Van Oyen et al., 2014):

$$\psi\left(\frac{d\xi}{dt}+\frac{\partial\zeta}{\partial t}\right)-\left[\frac{\partial}{\partial x}\left(\frac{K_s^2\phi^2}{UD}\frac{\partial\zeta}{\partial x}\right)+\frac{\partial}{\partial y}\left(\frac{K_s^2\phi^2}{UD}\frac{\partial\zeta}{\partial y}\right)\right]=0 \tag{3}$$

Here, U is the modulus of the depth-averaged velocity, K_s is the Gauckler-Strickler resistance coefficient, ψ and ϕ are two functions arising from the depth-averaging of the three-dimensional Reynolds equations over a representative elementary area to account for wetting and drying effects (Defina, 2000). Details about the numerical solution of the set of equations (1)-(3) are discussed in Geng et al. (2021).

Sediments are assumed fine enough to be transported mainly as suspended load. Their dynamics are thus described by the two-dimensional advection-dispersion equation (D'Alpaos et al., 2007):

$$\frac{\partial(CD)}{\partial t}+\nabla(CDU-k_mD\nabla C)=Q_e-Q_d \tag{4}$$

where C is the depth-averaged suspended sediment concentration, k_m is the horizontal mixing coefficient, and Q_e and Q_d are the rate of erosion and deposition, respectively.

The sediment balance equation (Exner equation) takes the form (Marani et al., 2010; Toffolon & Lanzoni, 2010)

$$\frac{\partial z_b}{\partial t}=Q_e-Q_d \tag{5}$$

where z_b is the local bed elevation relative to a given constant mean sea level (MSL).

The erosion flux is assumed to depend on the excess of local shear stress with respect to the critical stress according to the relation proposed by Carniello et al. (2012). The deposition flux includes sediment settling and, in the presence of vegetation, sediment trapping, and organic soil production. Settling is modeled as the product of sediment concentration by settling velocity. Trapping deposition and organic production rates are related to vegetation biomass through the relations provided by Palmer et al. (2004) and Mudd et al. (2004).

Vegetation growth is modeled through a biomass function, which correlates the annually-averaged biomass density B to the local bed elevation z_b, namely

$$\frac{B(z_b)}{B_{max}}=b(z_b)=\frac{f(z_b)}{f_{max}} \tag{6}$$

where B_{max} is the maximum biomass density and $f(z_b)$ is a fitness function (Marani et al., 2013) with maximum value f_{max}.

Besides sediment deposition, vegetation also influences the flow resistance. The overall bed friction is given by the sum of the local bed friction and the vegetation-induced friction. The Gauckler-Strickler resistance coefficient is thus expressed as

$$K_s^{-2}=K_{sb}^{-2}+bK_{sv}^{-2} \tag{7}$$

where K_{sb} and K_{sv} are the Gauckler-Strickler coefficients related to bed friction and vegetation, respectively.

Table 1. Relevant relations and values of the corresponding parameters adopted in the simulations. Sources: [1]D'Alpaos et al. (2007); [2]Mudd et al. (2004); [3]Carniello et al. (2012); [4]Marani et al. (2013); [5]Palmer et al. (2004); [6]D'Alpaos et al. (2006); [e]Geng et al. (2021); [8]van Oyen et al. (2008); [9]Gibbs (1985); [10]Fagherazzi and Furbish (2001); [11]Belliard et al. (2015)

Parameter	Relation	Short description	Parameter	Relation	Short description
Q_d	$Q_{ds} + Q_{dt} + Q_{do}$	Total deposition rate[1]	Q_{ds}	Cw_s	Settling deposition rate[2]
Q_{do}	$Q_{do0} b(z_b)$	Organic production rate[2]	Q_{dt}	$CU\varepsilon_v d_v n_v min[h_v; D]$	Trapping deposition rate[1]
Q_e	$Q_{e0}\left\{-1+\left[1+\left(\frac{\tau}{\tau_{ce}}\right)^4\right]^{1/4}\right\}$	Erosion rate[3]	$f(z_b)$	$\frac{2}{e^{[\lambda_1(z_b-z_{0v})]}+e^{[-\lambda_2(z_b-z_{0v})]}}$	Vegetation fitness function[4]
ε_v	$\alpha_\varepsilon\left(\frac{Ud_v}{\upsilon}\right)^{\beta_\varepsilon}\left(\frac{d_{50}}{d_v}\right)^{\gamma_\varepsilon}$	Capture efficiency coefficient[5]	d_v	$\alpha_d B^{\beta_d}$	Stem diameter[6]
n_v	$\alpha_n B^{\beta_n}$	Stem density per unit area[6]	h_v	$\alpha_h B^{\beta_h}$	Average stem height[6]
τ_{ce}	0.4 Pa	Critical erosion stress[6]	g	9.81 m/s^2	Gravity acceleration
k_m	0.3 m^2/s	Horizontal mixing coefficient[1]	w_s	0.0002 m/s	Settling velocity of sediment particles[1]
Q_{e0}	0.0002 m/s	Typical intensity of erosion flux[7]	Q_{do0}	0.003 m/yr	Typical organic production rate[7]
K_{sb}	25 m$^{1/3}$/s	Gauckler-Strickler coefficient for bed friction[8]	K_{sv}	10 m$^{1/3}$/s	Gauckler-Strickler coefficient for vegetation[8]
ρ	2650.0 kg/m^3	Sediment density	d_{50}	50 μm	Median sediment size[6]
υ	0.000001 m^2/s	Kinematic viscosity of water	α_ε	0.224	Empirical coefficient[5]
β_ε	0.718	Empirical coefficient[5]	γ_ε	2.08	Empirical coefficient[5]
α_n	250 g^{-1}	Empirical coefficient[2]	β_n	0.3032	Empirical coefficient[2]
α_h	0.0609 m^3/g	Empirical coefficient[9]	β_h	0.1876	Empirical coefficient[10]
α_d	0.0006 m^3/g	Empirical coefficient[9]	β_d	0.3	Empirical coefficient[10]
λ_1	1 m^{-1}	Scale parameter controlling vegetation fitness variation rate[4]	λ_2	36 m^{-1}	Scale parameter controlling vegetation fitness variation rate[11]
z_{0v}	0.2032 m	Elevation parameter corresponding to the optimal elevation[4]	f_m	40 (tidal cycle < 100) 200 (tidal cycle ≥ 100)	Morphological factor[7]

The hydrodynamics and the bed evolution are assumed to be characterized by different temporal scales. The flow field is taken to adapt almost instantaneously to changes in bed

elevation and, hence, equations (1)-(4) are solved separately from equation (5). At each time t of a characteristic tidal cycle, equation (3) is solved to obtain the spatial distribution of the variation of free surface elevation $\zeta(x, y, t)$ and, through equations (1) and (2), the corresponding values of the depth-averaged velocity components. The free-surface elevation is then used to determine the bed shear stress components

$$\tau_x = -\rho g D \frac{\partial \zeta}{\partial x}, \quad \tau_y = -\rho g D \frac{\partial \zeta}{\partial y} \tag{8}$$

needed to compute the local values of the erosion and deposition fluxes and, by solving equation (4), the suspended sediment concentration.

At the end of any characteristic tidal cycle, the bed elevation is updated by employing the tidally-averaged erosion/deposition rates multiplied by a morphological acceleration factor (f_m). The characteristic tidal cycle is then repeated.

Vegetation biomass is computed as a function of bed elevation through equation (6). It affects the morphological evolution by increasing deposition fluxes by sediment trapping and organic soil production, reducing to zero erosion fluxes, and enhancing the resistance to the flow as described by equation (7).

The specific relations used to compute the sediment fluxes and the fitness function for vegetation, as well as the relevant parameters used in the eco-morphodynamic model, are summarized in Table 1. In general, the adopted relations and the values of the parameters therein stem from consolidated analyses carried out throughout the years by coupling numerical modeling and field observations. Here, we use the parameter set adopted by Geng et al. (2021) to investigate the eco-morphodynamic evolution of intertidal areas fringing a main channel and of the tidal creeks cutting through them, validated though a general comparison with the channel patterns observed in Warbah Island (Kuwait) and in the Venice lagoon (Italy). However, differently from Geng et al. (2021), here we consider a single fitness function characterized by a biomass distribution with a wide adaptation range typical of a multi-species scenario (e.g., Marani et al., 2013).

2.2 Design of numerical experiments

In the absence of externally-imposed overtides, the water elevation at the sea boundary $\xi(t)$ simulates a semidiurnal (S2) tide typical of micro-tidal environments, i.e., with a period of 12 h and an amplitude of 0.75 m referred to MSL of 0 m. A relaxation procedure has been employed to reduce the scouring potential in the early stages of morphodynamic evolution and, hence, to avoid spurious numerical instabilities. The tide amplitude is , in fact, allowed to gradually increase from 0 to 0.75 m within the first 800 tide cycles (corresponding to about 1.1 yr) to avoid intense erosion processes near the seaward boundary at the beginning of each simulation. On the other three boundaries of the tidal basin, a no-flux condition is enforced (Figure 2a). At the beginning of the simulation, the high water slack level is prescribed throughout the basin, while the flow velocity is set everywhere to zero. The simulation thus starts with the ebb phase.

In this contribution, the effects of overtides are investigated by adding to the main semidiurnal constituent (S2), the quarter-diurnal (S4), and sixth-diurnal (S6) constituents, with amplitudes and phases chosen to reproduce either flood-dominated or ebb-dominated conditions (Table 2). The water elevation at the sea boundary then reads:

$$\xi(t) = \sum_{i=1}^{3} A_i cos(\sigma_i t - \upsilon_i) \quad (9)$$

where A_i is the tidal amplitude of the i-th constituent, while σ_i and υ_i are the corresponding tidal frequency and phase shift, respectively. The values of these quantities have been chosen such that the flooding period is half of the ebb period in the flood-dominated case, and vice versa in the ebb-dominated case.

Table 2. Values of tidal constituents used to reproduce either a flood-dominant or an ebb-dominant tidal forcing at the sea boundary.

Tidal forcing	Constituent	A_i (m)	T (h)	σ_i (deg/h)	υ_i (deg)
Flood-dominant	S2	0.7286	12	30	30
	S4	0.1314	6	60	330
	S6	0.0429	4	90	270
Ebb-dominant	S2	0.7286	12	30	330
	S4	0.1314	6	60	30
	S6	0.0429	4	90	90

A suspended sediment concentration C_{sea} = 0.01 kg/m^3 is prescribed at the seaward boundary during the flood phase to mimic an external sediment input. Conversely, as the suspended sediment leaves the tidal basin during the ebb phase, the sediment concentration at the seaside boundary is taken to be determined by the local transport capacity. At the beginning of the simulation, the suspended-sediment concentration within the basin is assumed to decrease linearly from C_{sea} at the seaward boundary to 0 at the landward boundary.

To simulate different initial bed conditions, some perturbations, mimicking natural micro-topography variations, were superposed to an otherwise horizontal intertidal platform (Figures 2a,c). According to the fitness function adopted in this study, vegetation starts to grow as soon as bed elevation exceeds the mean sea level (Figure 2d). The slightly-increased elevation associated with bed perturbations thus promotes the establishment of vegetation, and the perturbations can be taken to mimic heterogeneous vegetation encroachment on the intertidal platform (Figure 1). Both the position and magnitude of each perturbation were determined randomly following the procedure described in Geng et al. (2021). First, the location (x,y) of each perturbation and the corresponding height are selected randomly. Second, the elevation around the selected location is averaged iteratively to generate a bump with a smoothly varying surface. The procedure is repeated several times (15 in the considered cases) to increase the bump extension while reducing its height. Finally, the maximum elevation of the resulting bed topography is set equal to 0.1 m, and the height of other points is adjusted proportionally. The bed topography thus generated is characterized by relatively isolated irregularities with some clustered patterns (Figure 3).

The initial bed configurations considered in the various simulations are listed in Table 3. A more perturbed initial bed surface were obtained by increasing the number (hereafter density) of perturbations (Figures 3a,b,c), with a consequent change also in the Probability Density Function (PDF) of initial elevation (Figure 3m). On the other hand, for a given PDF, determined

by the number and size of the assigned bed perturbations, different spatial distributions (i.e., locations) of perturbations (Figures 3d,e,f, and 3g,h,i) can be obtained by random sampling the assigned PDF (Figures 3n,o). Specifically, configurations #1 to #3 (Figures 3a-c) were obtained using low, medium and high densities, respectively. Configuration #2 was produced by adding 200 new randomly-generated bumps to configuration #1. Similarly, configuration #3 was obtained from configuration #2, introducing 200 further randomly-generated bumps. The associated PDFs change since the frequency of higher elevation increases in the cases with denser perturbations (Figure 3m). Configurations #4 to #9 (Figures 3d-i) were generated to analyze the consequences of different spatial distributions of perturbation characterized either by sparse (Figures 3d-f) or clustered (Figures 3g-i) bed irregularities. These bed topographies were created randomly and independently, maintaining the same PDFs shown in Figures 3n and 2o.

Another topographic factor considered in this study is the initial slope of the intertidal platform. In the case of a horizontal intertidal platform, the base elevation is set at 0 m above MSL. For sloping intertidal platforms, the elevation is assumed to increase landward, thus leading to a seaward sloping bed. The effects of a sloping bed were investigated with reference to the initial configurations #10 (slope of 0.075 %, Figures 3k) and #11 (0.125 %, Figure 3l) as compared to the horizontal bed configuration #2 (Figures 3b and 3j). Random initial bed perturbations were, as usual, superposed to the sloping bed surface. The density and spatial distribution of perturbations in the sloping bed configurations (#10 and #11) were identical to those used for configuration #2. Finally, the contributions of either flood-dominant (Run #12) or ebb-dominant tides (Run #13) were analyzed by using the initial bed configuration #2.

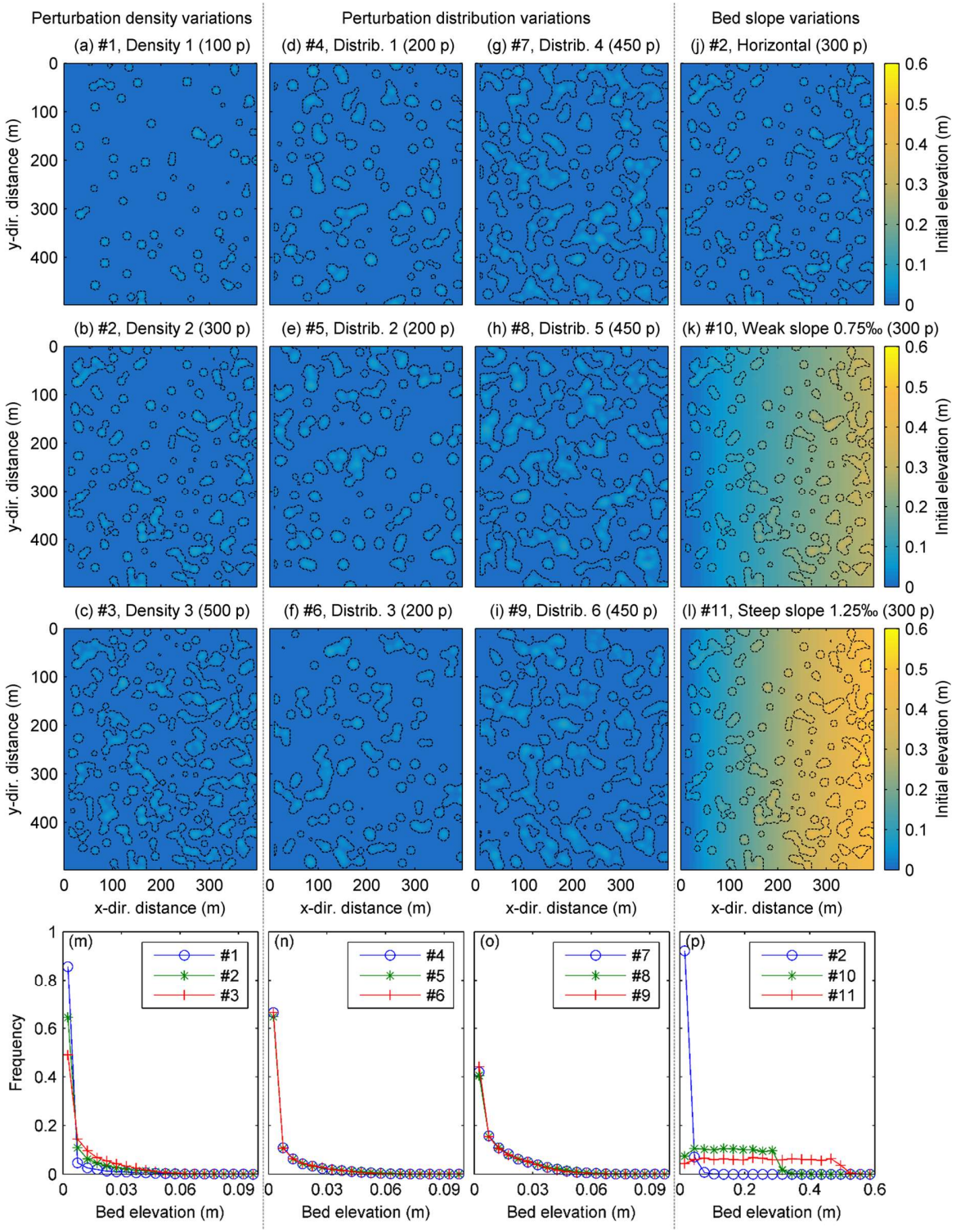

Figure 3. Initial irregular bed topographies used in the present simulations by varying (**a-c**) perturbation density, (**d-i**) perturbation distribution, and (**j-l**) bed slope. The black dotted lines in panels (**a-l**) denote the range of initial bed perturbations. The corresponding PDF of bed

328 elevation in the four groups are shown in panels (**m-p**). Note that the range and the interval of
329 the x-axis in panel (**p**) are different from the other three panels.

330

331 **Table 3.** List of simulations carried out to analyze the effects of initial conditions. Note that the
332 maximum height of perturbations is always equal to 0.1 m, but the frequency distributions can
333 vary, as shown by the PDF plots of Figures 3m-p.

Run	Initial bed perturbation	Number of perturbations	Bed slope	Soil cover	Tidal forcing
#1	low/medium/high perturbation densities	100 p	0	Vegetated & Unvegetated	S2
#2*		300 p	0	Vegetated & Unvegetated	S2
#3		500 p	0	Vegetated & Unvegetated	S2
#4	sparse perturbations with same density but different locations	200 p	0	Unvegetated	S2
#5		200 p	0	Unvegetated	S2
#6		200 p	0	Unvegetated	S2
#7	clustered perturbations with same density but different locations	450 p	0	Unvegetated	S2
#8		450 p	0	Unvegetated	S2
#9		450 p	0	Unvegetated	S2
#10	medium perturbation density	300 p	0.075%	Vegetated & Unvegetated	S2
#11		300 p	0.125%	Vegetated & Unvegetated	S2
#12	medium perturbation density	300 p	0	Unvegetated	Flood-dominant (S2+S4+S6)
#13		300 p	0	Unvegetated	Ebb-dominant (S2+S4+S6)

334 Note. Run #2 is set up as the Reference Case. Runs #4 to #6 are different realizations of random sampling from the
335 PDF of Figure 3n. Runs #7 to #9 are different realizations of random sampling from the PDF of Figure 3o.

336 Both vegetated and unvegetated conditions have been considered to highlight the role
337 exerted by halophytic plants on the morphodynamic evolution of the tidal basin. In the vegetated
338 cases, a vegetation scenario with multi-species has been studied. Overall, vegetation (i.e., the
339 combination of different species) is assumed to encroach a relatively wide range of elevations,
340 mimicking the biomass dynamics occurring in some salt marshes of the Venice Lagoon (Marani
341 et al., 2004). Specifically, vegetation is assumed to grow when the bed elevation exceeds MSL
342 (Da Lio et al., 2013), with a biomass density depending on the local elevation according to the
343 distribution shown in Figure 2d. The corresponding fitness function (Equation 6) and the relevant
344 parameters are those reported in Table 1. Overall, the slightly higher elevations characterizing
345 the initially perturbed bed can be regarded as newly-formed pioneer vegetation patches (Figures
346 1 and 2a). Changing the initial perturbation density (cases #1 to #3) is then equivalent to
347 simulating the evolution of the tidal platform colonized by different amounts of vegetation
348 patches.

Note that the vegetation scenario considered in the simulations is characterized by biomass production that increases quite rapidly as soon as the tidal platform exceeds 0.1 m above MSL. It reaches a maximum at 0.3 m above MSL and then decreases slowly (Figure 2c). Vegetation thus has a strong impact on the growth of the tidal network, owing to the significant and prolonged influence on the morphodynamics of the tidal system.

Each simulation lasted 115 yr, a period of time long enough to ensure that sediment erosion and deposition rates eventually balance out, i.e., the net entrainment rate of bed sediment approaches zero. Hence, at the end of the simulation, the channel network morphology reached an asymptotical equilibrium condition whereby bed level changes tended to vanish (Zhou et al., 2017). The build up of elevation near the seaward border progressively limit the amount of sediment that the basin exchanges with the sea. The bed topography of inner areas adapts such that the net rate of entrainment of bed sediments, on average, tends to vanish.

3 Results

First, we study the effects of initial bed irregularities on channel development and the final tidal network morphology in the absence of vegetation. Next, we will discuss how vegetation affects tidal channel dynamics in the case of both horizontal and sloping initial bathymetry. In all the investigated cases, after the initial formation of tidal channels, channelled areas are extracted following the procedure described in Geng et al. (2018) based on the comparison of relative elevations of neighboring areas. This method has been demonstrated to be fairly robust in delineating the structure of creek networks in intertidal zones with complex topographies and rapidly varying flow fields as those investigated in the present contribution. The channel network morphologies obtained in the various simulations are then compared in terms of channel length, unchannelled path length, relative drainage efficiency, and total channel network volume.

The total channel length L_c includes all the channels generated within the tidal basin. The channel volume V_c is defined as the integral of the cross-section area along the channel axes. The drainage efficiency of a tidal channel network is here defined as the ratio l_H/l of the Hortonian characteristic path length l_H to the mean unchannelled flow length l, a distinctive measure of the overall channel network features (Marani et al., 2003). Denoting by A_b the area of the entire tidal basin and noting that $l_H = A_b/L_c$ is the inverse of the drainage density, the drainage efficiency can be computed as $l_H/l = A_b/(L_c l)$. High values of l_H/l for a given l_H correspond to small values of l, i.e., to a spatial arrangement of channels, which efficiently reduces the mean unchanneled path length, enhancing the drainage efficiency.

Although the drainage efficiency is a metric able to discriminate between different branching structures and meandering characteristics (Marani et al., 2003; Kearney and Fagherazzi, 2016), we evaluated also the Strahler Stream Order (Strahler, 1952) of the various channels and the number of branching points to further quantify the complexity of the simulated networks.

3.1 Effects of the initial bathymetry on the growth of tidal networks dissecting tidal flats

The final asymptotic equilibrium configurations of the tidal basin are shown in Figure 4. Table 4 compares the number of channels with different Strahler Stream Order and the branching points in all the simulated cases.

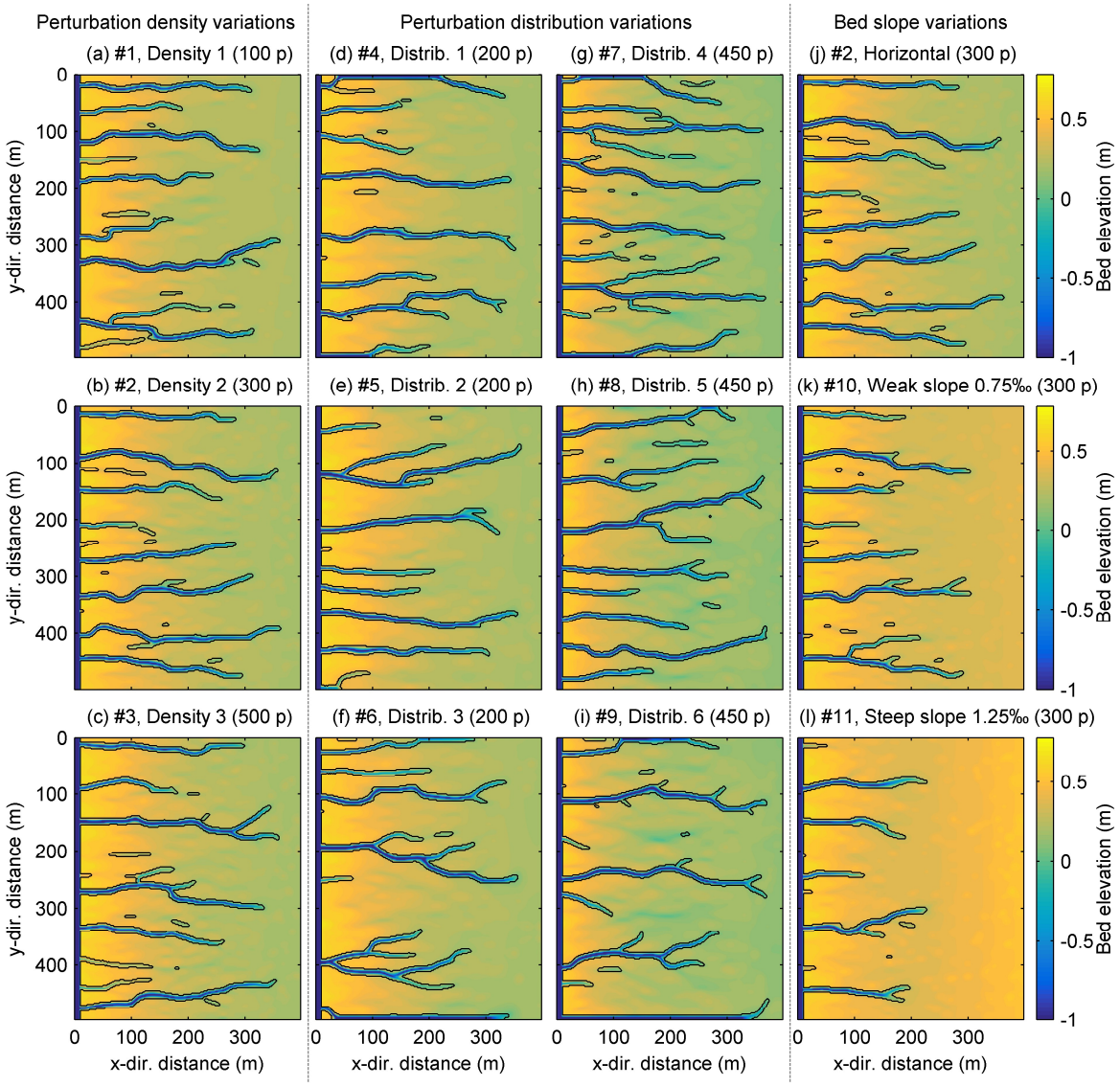

Figure 4. The spatial distribution of bed elevation is plotted for the simulations carried out in the absence of vegetation for the initial bathymetries shown in Figure 3. Black lines denote the edge of tidal channels.

Table 4. The number of channels with different Strahler Stream Order (SSO) and the number of branching points in the simulated tidal networks. Channels (or branches) shorter than 8 m have been neglected.

	Run #1 No vege	Run #2* No vege	Run #3 No vege	Run #4 No vege	Run #5 No vege	Run #6 No vege	Run #7 No vege	Run #8 No vege	Run #9 No vege
SSO 1	10	12	11	11	11	13	15	13	15
SSO 2	1	2	2	2	2	4	3	3	3
SSO 3	0	0	0	0	0	1	0	0	0

Scattered channel	4	4	4	1	1	2	5	2	3
Branching point	1	2	3	3	3	6	5	4	7
	Run #10 No vege	Run #11 No vege	Run #12 No vege	Run #13 No vege	Run #1 Vege	Run #2* Vege	Run #3 Vege	Run #10 Vege	Run #11 Vege
SSO 1	12	8	16	16	20	21	26	23	15
SSO 2	2	2	3	4	7	6	7	6	5
SSO 3	0	0	0	0	1	1	2	1	1
Scattered channel	1	1	6	0	4	12	8	3	4
Branching point	4	2	5	5	11	11	16	13	7

Note. Run #2 is set up as the Reference Case. Scattered channels denote the channels disconnecting with the deep seaward channel.

The evolution of the tidal network proceeds similarly in all the cases. At the beginning of evolution, several channels are generated at the seaward boundary and then extend landward through headward erosion. In-channel erosion increases sediment availability, leading to an intense deposition close to the seaward boundary where the intertidal platform progressively attains elevations higher than in inner areas. Extending landward, channels start winding and branching due to the complex flow field favoured by perturbation patches. Changing the density of initial bed irregularities does not remarkably affect the complexity of the tidal system (Figures 4a-c). Indeed, the number of channels and their orientations are approximately the same (Table 4, runs #1 to #3). On the other hand, differently-distributed initial perturbations lead to more significant changes in channel morphology (Figures 4d-f and 4g-i as compared to Figures a-c) and the number of channels (Table 4, runs #4 to #9). In the cases of a sparse distribution (runs #4 to #6), the channel structure obtained in run #6 (Figure 4f) is characterized by unevenly-distributed channels with more branches and high Strahler stream-order channels as compared to the channels obtained in runs #4 and #5 (Figures 4d-e, and Table 4 runs #4 to #6). The uneven distribution of channels achieved in run #6 carries the trace of the random initial perturbations, with some transversally (y-directionally) extended perturbation patches that tend to limit channel growth. Overall, different randomly-generated distributions of perturbations of the initial bathymetry (runs #4-#9) generate networks with different channel complexity, leading to significant variations in quantities of channels and branching points.

The effect of a sloping channel bed emerges clearly from the asymptotic equilibrium bed configurations shown in Figures 4j-l. Almost parallel channels with similar spacing were generated in the presence of either a horizontal platform (run #2, Figure 4j) or sloping platforms (Figures 4k,l). However, a steeper bed surface leads to shorter channels. Moreover, the landward upper portion of the tidal basin almost fills in by the end of the run (Figures 4k and 4l). The mild channel lengthening shown in runs #10 and #11 is strictly related to the reduction of the tidal prism, as it will be discussed in Section 4.1.

3.2 Effects of the initial bathymetry on the growth of tidal networks dissecting salt marshes

The development of salt marshes adds a further degree of complexity to the morphodynamic evolution of tidal networks. Considering the initial distribution of bed irregularities in run #2 (Figure 3b), we first compare the basin bathymetries obtained at different stages of evolution (4, 12, 45, and 115 yr) in the presence/absence of vegetation (Figures 5a-h). The corresponding spatial distributions of vegetation biomass are shown in Figures 5i-5l.

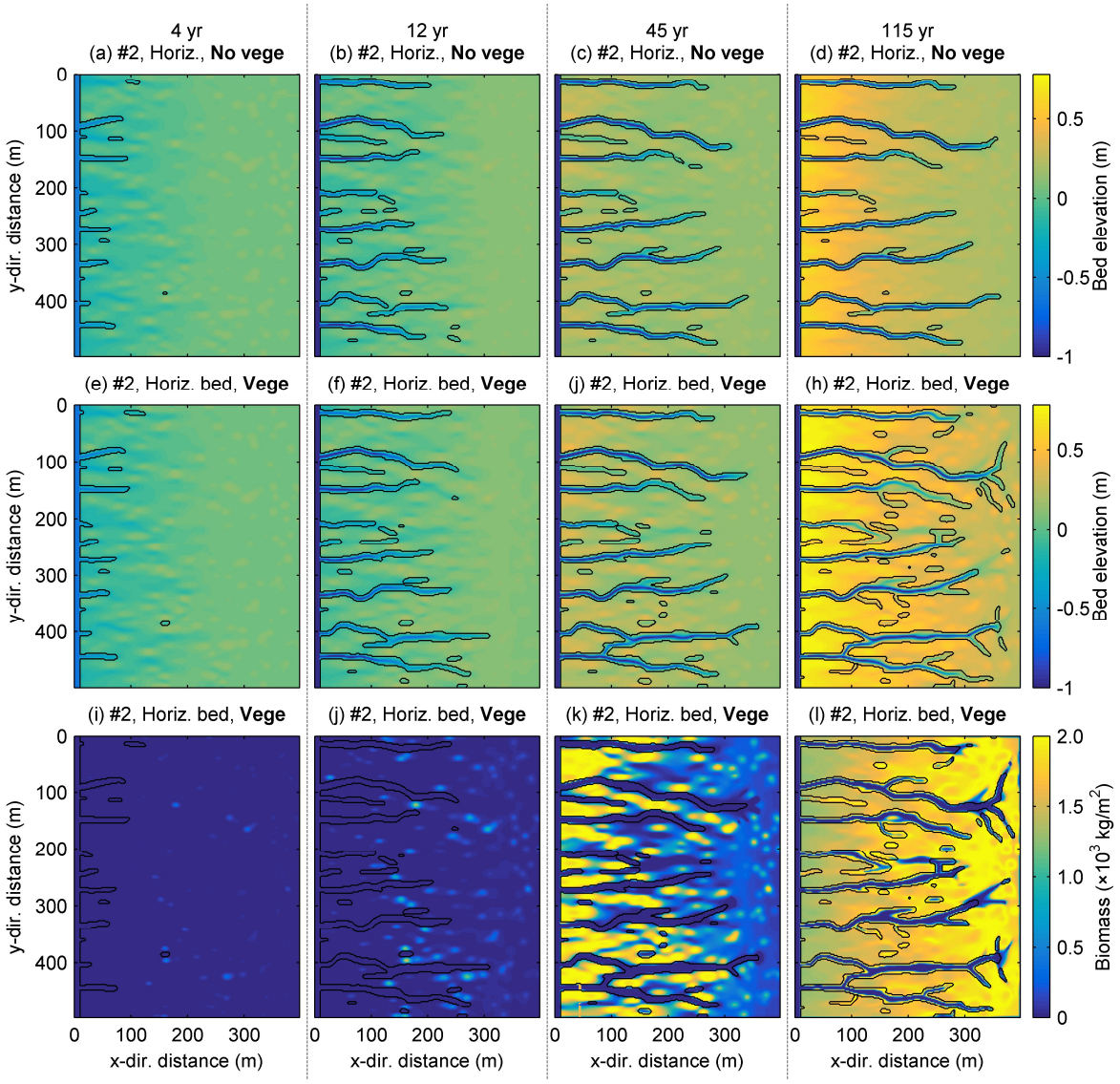

Figure 5. The spatial distribution of bed elevations in run #2 (Figure 3b) is plotted at different evolution stages (4, 12, 45, and 115 yr) in the absence (**a-d**) and in the presence (**e-h**) of vegetation. The corresponding spatial distribution of biomass is plotted in panels (**i-l**). Black lines denote the edge of tidal channels.

Similar morphodynamic trends are observed in the presence/absence of vegetation. Several short channels form at the seaward boundary after about 4 yr (Figures 5a and 5e). During this early evolution stage, erosion tends to lower the seaward area, limiting the growth of vegetation. Therefore, little difference is observed in channel patterns formed with and without vegetation (Figures 5a and 5e). After channel initiation, erosion occurs in channelled areas, while unchannelled areas are dominated by deposition. Vegetation patches start to grow after 12 yr in the middle of the tidal basin, where the most intense net deposition takes place (Figure 5j). As the seaward portion of the basin rises to a sufficiently high elevation (45 yr), salt marshes

gradually extend seaward (Figure 5k), eventually covering the entire basin (Figure 5l). Trapping deposition and organic soil production lead, on average, to higher basin elevations and longer channels with more branches (Figure 5h and Table 4, run #2 with vegetation) as compared to unvegetated conditions (Figure 5d and Table 4, run #2 without vegetation).

To analyze the mutual interactions between vegetation growth and bed evolution, the temporal and spatial biomass variations obtained with different perturbation densities (runs #1 to #3) are compared in Figure 6.

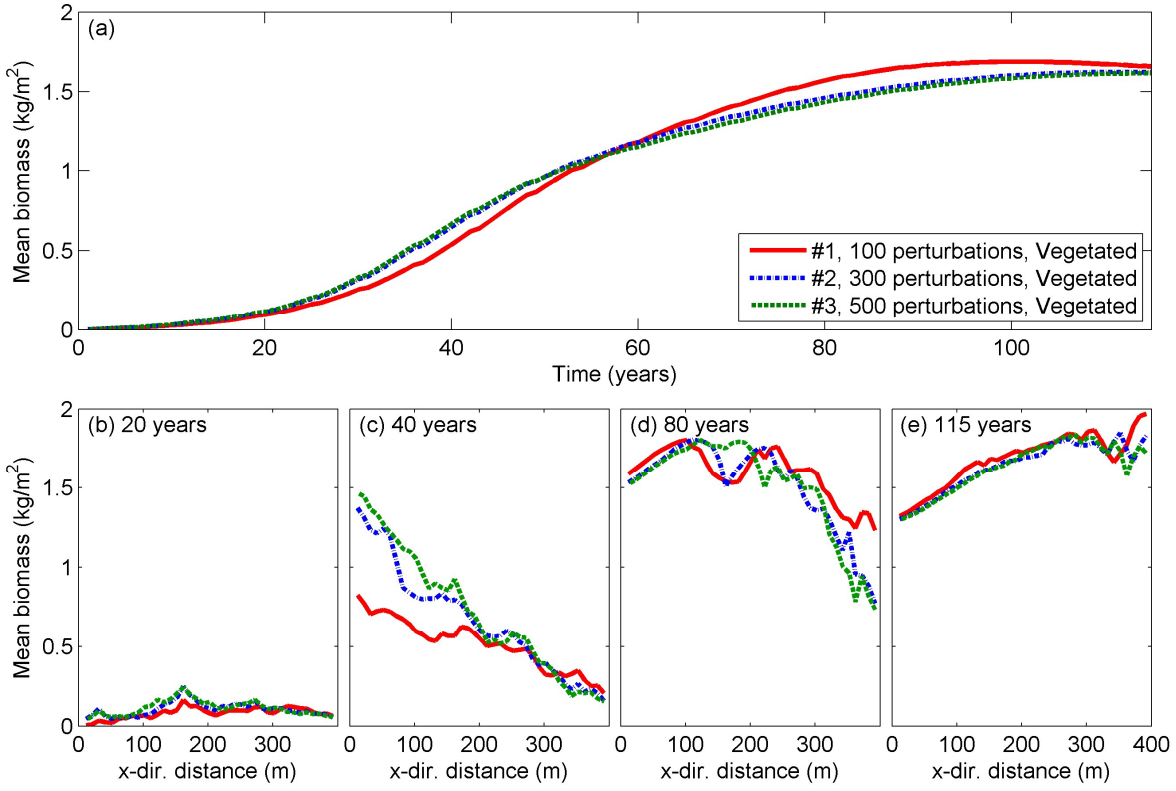

Figure 6. (**a**) The variation of the mean biomass over the entire basin is plotted as a function of time in the three vegetated cases. (**b-e**) The longitudinal distribution of the mean (transversally-averaged) biomass density is plotted at different evolution stages (20, 40, 80, and 115 yr) for different densities of the initially imposed perturbations. Red, blue and green lines refer to initial bed surfaces with 100, 300, and 500 perturbation patches, respectively.

During the first 65 years, denser initial perturbations lead to faster growth of the total biomass over the entire basin (green and blue lines in Figure 6a). Later on, the total biomass obtained for less dense perturbations (run #1) exhibits a more rapid increase (red line in Figure 6a). The different evolution stages shown in Figure 6a arise from the diverse evolution rates experienced by different areas of the tidal basin. For this reason, in Figures 6b-e, we compared the longitudinal distributions of the mean (transversally-averaged) biomass density at various stages of the evolution (20, 40, 80, and 115 yr).

As the seaward platform elevation increases, denser vegetation patches contribute to a faster biomass growth(Figure 6c). However, in the landward portion of the basin, the mean biomass always remains higher for the lowest number of initial perturbation patches (Figures 6c and 5d, red lines). This happens because a large amount of suspended sediment is trapped by well-developed seaward vegetation patches, which form in runs #2 and #3. Less sediment is then delivered to inner areas, leading to a weaker deposition and, hence, lower bed elevations in the landward regions. Indirect evidence can be found in the field observation of Gong et al. (2017), which shows that bed accretion attains its maximum value in front of densely vegetated salt marshes and then decreases landward due to sediment trapping by vegetation. For this reason, when considering the entire basin, the total biomass in the denser-perturbation cases increases more slowly in the late stage of the evolution (Figure 6a, blue and green lines, after 60 years). On the other hand, after the seaward basin elevation exceeds the optimal elevation for vegetation growth, the slowly declining biomass production reduces the differences in seaward biomass observed in the three cases (Figures 6d and 6e). Overall, widely spread vegetation patches (associated with a denser distribution of initial perturbations) enhance the nonuniformity of biomass distribution from seaward to landward areas during the morphodynamic evolution of the tidal basin. Conversely, in the presence of a less dense distribution of initial perturbations, the reduction of seaward vegetation patches benefits vegetation growth landwards, and salt marshes eventually colonize the whole tidal platform much earlier than in the other cases.

3.3 Effects of the slope of the initial bathymetry on the growth of tidal networks

In the case of a flat initial bathymetry (Figures 5 and 6), salt marshes tend to first colonize the middle and seaward basin areas and then extend landwards. Meanwhile, tidal channels are generatedfrom the seaward boundary and then grow landward, indicating that the salt marsh extension proceeds consistently with tidal channel development both in space and time. The presence of a slope in the initial bathymetry can significantly affect this overall picture, as shown in Figure 7, which represents run #11 as an example.

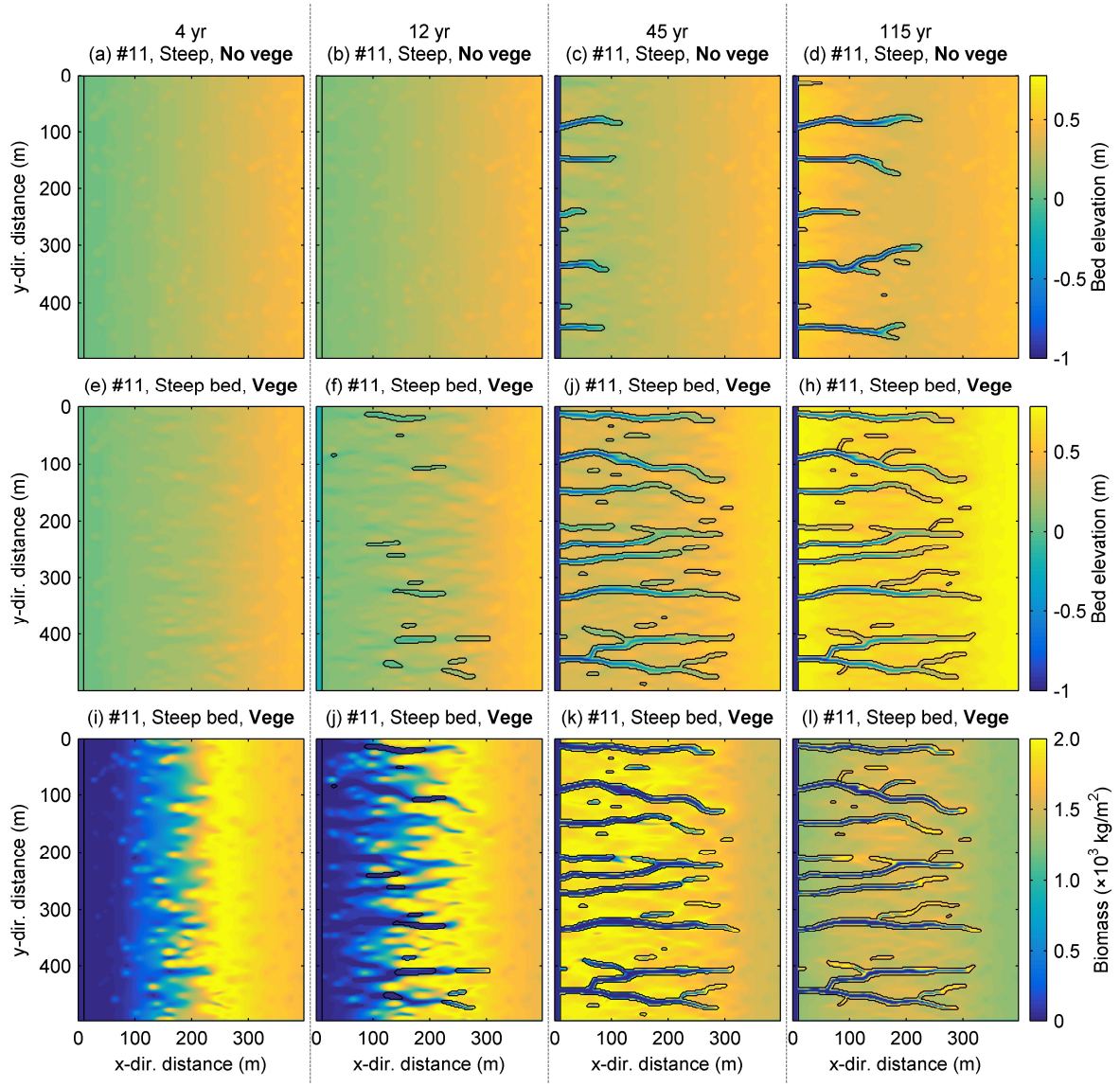

Figure 7. The spatial distribution of bed elevations is plotted at different evolution stages (4, 12, 45, and 115 yr) in the absence (**a-d**) and in the presence (**e-h**) of vegetation for the initial bed configuration #11 of Figure 3, characterized by a 0.125% longitudinal slope. The corresponding spatial distribution of biomass is plotted in panels (**i-l**). Black lines denote the edge of tidal channels.

In the absence of vegetation, the channels invariably develop at the seaward boundary and then extend landwards (Figures 7c,d). However, the formation of these channels is delayed with respect to the horizontal bed case (Figure 5a,b). Salt marshes, in fact, first colonize the most landward basin areas with higher initial bed elevations and then extend towards the initially deeper seaward areas (Figures 7i-7l). At the end of the simulation, the local bed elevation exceeds the optimal elevation for vegetation growth (Figure 7h). Thus, the biomass density reaches a value smaller than what is experienced at the intermediate evolution stages.

513 Vegetation encroachment favours the growth of some channels in the middle of the tidal
514 basin (x = 100~200 m) after 12 yr (Figure 7f), instead of initiating from the seaward boundary,
515 as typically observed in the cases of a flat initial bathymetry. These channels develop at the
516 border of salt marshes and unvegetated flats, where vegetation patches are distributed unevenly,
517 and tidal currents concentrate between the patches. In the following stages of evolution, the
518 channels gradually connect to the sea and, at the same time, grow landward by cutting through
519 the already existing salt marshes. At the landward head of the channel, sediment deposition on
520 the tidal platform promoted by vegetation exceeds in-channel erosion, eventually leading to
521 shallower channels and higher banks (Figure 7h).

522 3.4 Effects of overtides on the growth of tidal networks

523 The effects of overtides have been investigated with reference to the bathymetry #2
524 (Figure 3b) and in the absence of vegetation. Figure 8 shows the variation of the bed
525 topographies obtained when imposing either a flood-dominated or an ebb-dominated tidal
526 forcing due to external quarter-diurnal (S4) and sixth-diurnal (S6) overtides, as compared to the
527 bed topography resulting from the application of a symmetrical S2 forcing.

528 In the flood-dominated case, multiple scattered channel reaches form within the basin
529 (Figure 8a-d and Table 4, run #12). Conversely, in the ebb-dominated case (Figures 8i-l and
530 Table 4, run #13), the channels grow much faster, and no scattered channel reach is generated.
531 The differences in the morphodynamic evolution suggest that ebb currents are more efficient in
532 driving headward erosion, while strong flood currents may lead to more localized erosion
533 throughout the tidal basin. To determine the effects of flood- and ebb-dominant tide currents, we
534 compared the temporal variations of overall channel features (Figure 9).
535
536

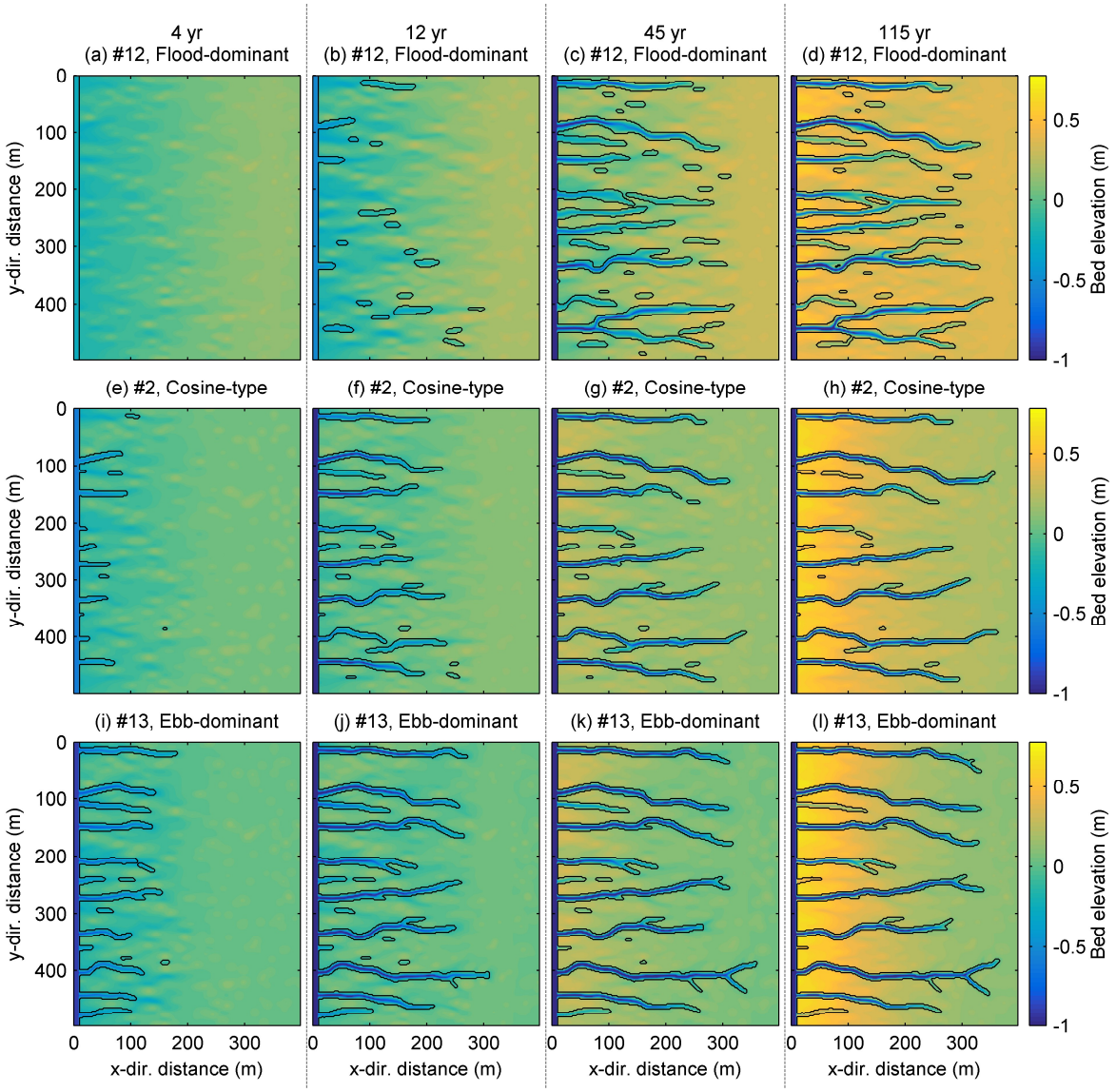

Figure 8. The spatial distribution of bed elevation of run #2 is plotted at different evolution stages (4, 12, 45, and 115 yr) under a flood-dominated tidal forcing (**a-d**), a symmetrical S2 tide (**e-h**), and an ebb-dominated tidal forcing (**i-l**). Black lines denote the edge of tidal channels.

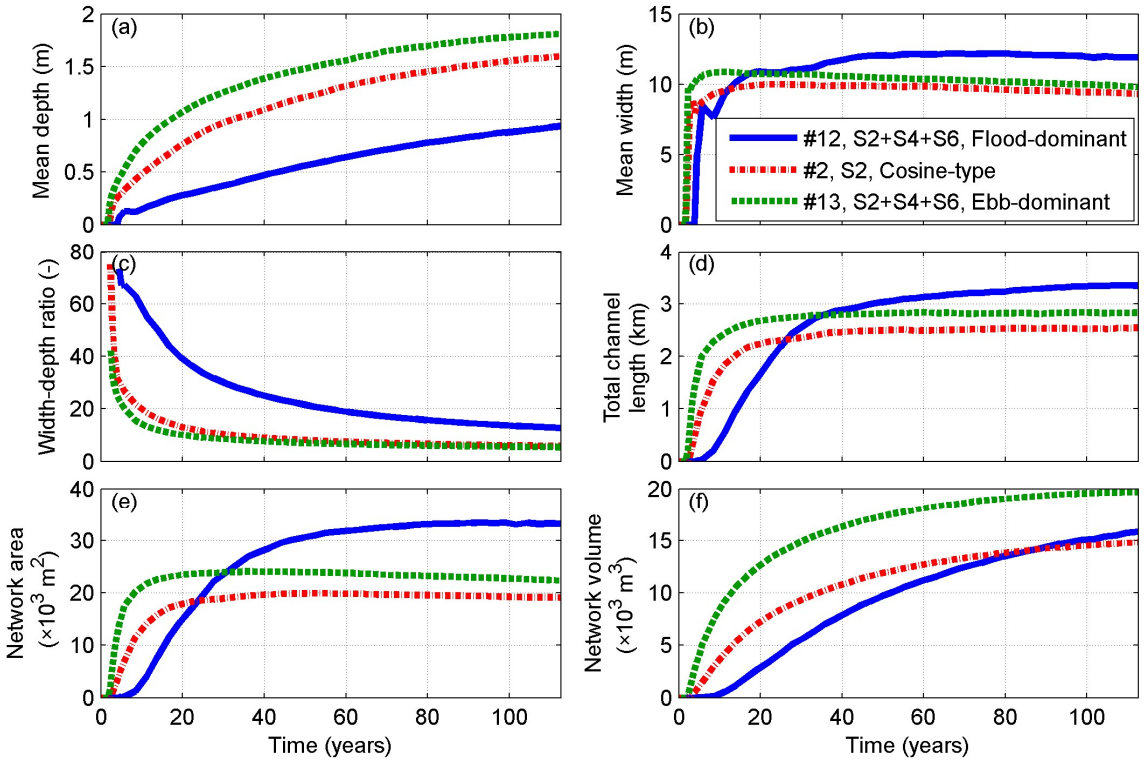

Figure 9. The temporal variations of (**a**) mean channel depth, (**b**) mean channel width, (**c**) mean width-depth ratio, (**d**) total channel length, (**e**) planar channel network area, and (**f**) channel network volume in the absence of externally imposed overtides (only S2 forcing) and in the presence of either flood-dominant or ebb-dominant externally imposed overtides (Table 2). Input parameters are the same as in runs #2, #12, and #13 in the absence of vegetation.

Imposing an ebb-dominated tidal forcing causes strong ebb currents, which promote channel deepening (Figure 9a), ultimately leading to smaller width-depth ratios as compared to the flood-dominated case (Figure 9c). Conversely, in the flood-dominated scenario, channels have wider cross sections (Figure 9b) and larger network areas (Figure 9e). These results are essentially due to the fact that, even though the flow tends to concentrate within the channels during the ebb phase regardless of the tidal asymmetry, the concentration is definitely stronger under ebb-dominated tides. In contrast, during the flood phase, water and sediment tend to spread out also throughout unchanneled areas. For flood-dominated tides, this leads to more evenly-distributed patterns, as well as wider and longer channels. However, although the channel length (Figure 9d) and the planar network area (Figure 9e) augment in the flood-dominated case, the network volume is still larger in the ebb-dominated scenario (Figure 9f), owing to the much deeper channels which form in this latter case.

4 Discussion

Our results provide a broad picture of the effects of the initial bathymetry and tidal conditions on the growth of tidal networks cutting through tidal flats or salt marshes. Here, we discuss whether the various equilibrium configurations follow any scaling relations. To this aim, below, we carry out overall quantitative comparisons among all cases, considering the tidal

prism-cross sectional area relation, the channel network volume, the mean unchannelled length, and the drainage efficiency.

4.1 Equilibrium state

The tidal prism–channel cross-sectional area ($P - A$) relationship has been originally developed to describe the overall effects of the mutual feedbacks between hydrodynamics, sediment dynamics, and morphology on the equilibrium of a tidal inlet. The relationship can be expressed by the power-law distribution:

$$A_e = kP^{\alpha} \tag{10}$$

where A_e is the minimum equilibrium cross-sectional area, computed with reference to MSL, P is the tidal prism (total volume of water conveyed by the corss section during a tidal cycle), while the coefficient k and the exponent α are typically determined from the plot of A_e versus P. The existence of relation (10) was initially inferred from field observations (O'Brien, 1969; Jarrett, 1976; Hume & Herdendorf, 1993) and subsequently confirmed by theoretical analyses (Marchi, 1990; Hughes, 2002; Tambroni & Seminara, 2009; D'Alpaos et al., 2009). Field data (Friedrichs, 1995), numerical simulations (D'Alpaos et al., 2010; van der Wegen et al., 2010), and physical experiments (Stefanon et al., 2010) showed that a relation similar to (10) also holds for sheltered tidal channels. Based on the empirical evidence gathered from tidal inlets worldwide, the exponent α has been found to range between 0.85 and 1.10 (Jarrett, 1976), while the empirical coefficient k may vary significantly in different coastal environments, depending on the hydrodynamics and the sediment grain size (D'Alpaos et al., 2009). A larger α implies a more significant effect of the tidal prism on the development of cross sections, and faster evolution of a tidal channel system.

Figure 10 compares the final relationships between the overall tidal prism (P) and the sum of the minimum cross-sectional areas (A_t) along the seaward boundary for all the simulated cases at the end of their evolution (after 115 yr). Note that, in this study, the simulated tidal basin is connected to the sea through multiple channels. Therefore, the area A_t shown in Figure 10 is the total seaward cross-sectional area measured below MSL at equilibrium. The corresponding tidal prism P then refers to the whole tidal basin. Although influenced by various initial conditions, the $P - A$ relationship in this study is invariably observed to follow well (coefficient of determination $R^2 = 0.918$) the power-law relationship (10) with $k = 9.11 \times 10^{-4}$ and $\alpha = 0.956$. The value of α falls within the range of empirical values reported in the literature (0.85-1.10). This confirms that channels have reached an equilibrium configuration characterized by a vanishing along-channel net sediment flux (D'Alpaos et al., 2010).

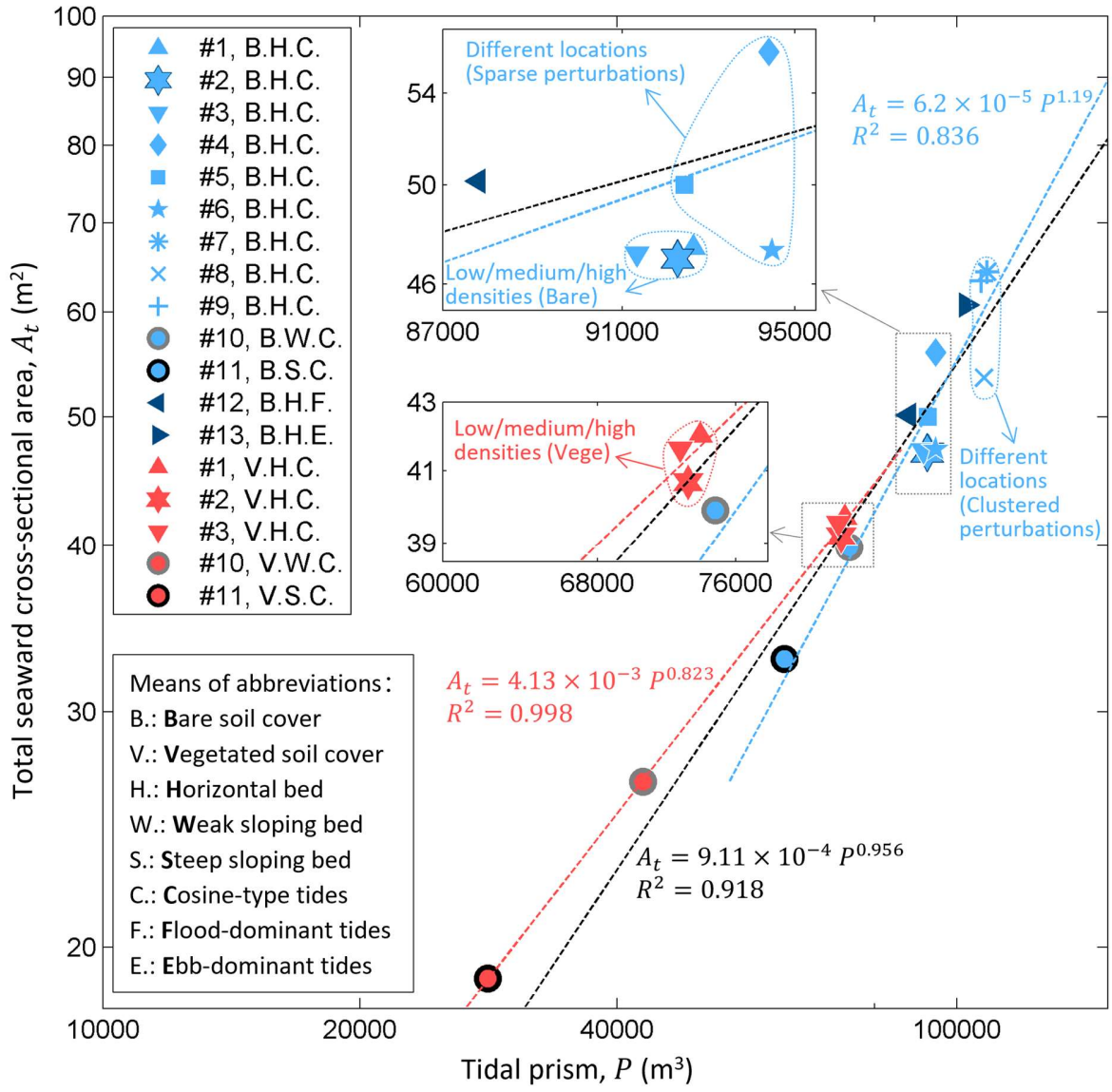

Figure 10. The sum A_t of the minimum seaward cross-sectional areas is plotted as a function of the overall tidal prism P for the equilibrium bed topographies. The various markers denote different settings for the initial bathymetry. Blue and red markers refer to unvegetated cases and vegetated cases, respectively. The markers with a grey edge identify the weakly sloping initial bathymetry (run #10), while markers with a black edge denote the steeply sloping initial bathymetry (run #11). The reference test (run #2) is denoted by hexagram markers with dark blue edges.

Changing the density (low/medium/high) of initial perturbations in both unvegetated and vegetated settings has a negligible influence on the final equilibrium configuration (Figure 10, runs #1 to #3). In contrast, different distributions of initial perturbations (sparse/clustered) may lead to a larger variability in the cross-sectional area (Figure 10, runs #4 to #9). In the presence of an initial sloping bathymetry, the tidal prism and the cross-sectional area get smaller values (Figure 10, runs #10 and #11 as compared to the reference run #2). Indeed, for a sloping

bathymetry, landward portions of the basin are flooded and drained less frequently by the tide. In turn, a landward-increasing bed surface reduces the tidal prism and, thus, the growth of the channel network, leading to less-developed (shorter) channels (Figures 4k and l). Finally, a flood-dominant tidal forcing (Figure 10, run #12) produces a smaller tidal prism as compared to the symmetrical tide adopted in run #2. This is due to the more intense sedimentation experienced by the basin, which, on average, leads to a higher mean elevation (Figure 8d) and a lower mean channel depth (Figure 9a). In contrast, an ebb-dominant tide determines a lower mean elevation (Figure 8l), a larger mean channel depth (Figure 9a), and, consequently, both a greater tidal prism and a bigger total cross-sectional area at the seaward border (Figure 10, run #13).

Fitting the points corresponding to vegetated and unvegetated cases separately, the exponent α takes the values 0.823 (red dashed line) and 1.19 (blue dashed line), respectively. This finding indicates that, in the absence of vegetation, the tidal channel system reaches an equilibrium state characterized by a larger rate of change of the equilibrium cross-sectional area as the tidal prism varies, and hence a higher sensitivity to changes in the hydrodynamics. Overall, the present results suggest that, besides tidal inlets and sheltered tidal channels, a $P - A$ scaling relationship could also be used to characterize the dynamic equilibrium of channels cutting through wetlands with an open seaward boundary. Clearly, this hint needs a thorough field validation which, however, is beyond the scope of the present study. In addition, we note that in our simulations, the prevailing sediment deposition near the seaward border tends to create an accreted belt of soil (Figure 4) which somewhat shelters the channels.

4.2 The drainage efficiency of tidal networks

Both the initial topography and the presence of vegetation affect the size of channels and their drainage abilities. However, channel systems exhibit various degrees of sensitivity to those factors. In Figure 11, the final channel network volume, the mean unchannelled length, and the drainage efficiency are plotted as a function of the total channel length for all the simulated cases.

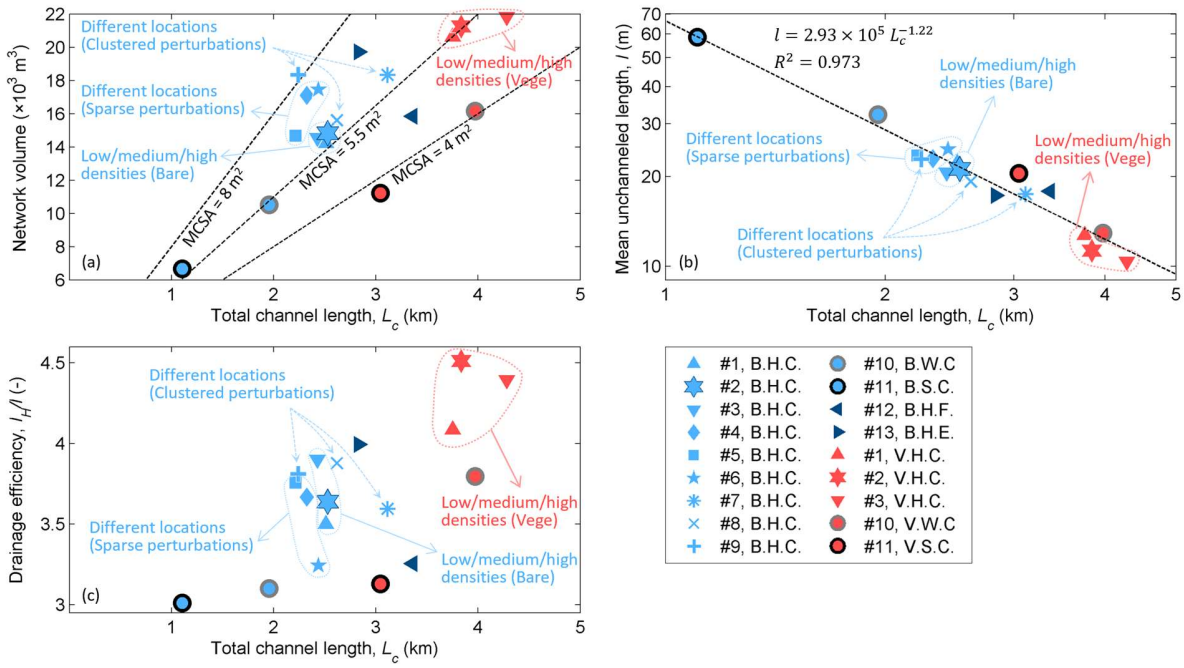

Figure 11. The (**a**) overall channel network volume, (**b**) mean unchannelled length (in double logarithmic coordinates), and (**c**) drainage efficiency are plotted as a function of the total channel length observed at the end of simulations. The various markers denote the different settings for the initial bathymetry. Blue and red markers refer to unvegetated and vegetated situations, respectively. The markers with grey edges denote weakly sloping initial bathymetry, while markers with black edges identify steeply sloping initial bathymetry. The reference test (run #2) is denoted by hexagram markers with dark blue edges. The dotted lines in panel (**a**) are obtained by using the mean cross-sectional area (MCSA) to compute the overall channel network volume.

The auxiliary dashed lines reported in Figure 11a have been obtained by computing the overall network volume for given values (8.0, 5.5, and 4.0 m^2) of the mean cross-sectional area (MCSA). The majority of data markers fall near the auxiliary line obtained for MCSA = 5.5 m^2. Deviations from this trend are observed for runs carried out with vegetation and a sloping initial bathymetry (Figure 11a, red circles with a grey or black edge). In these cases, vegetation leads to smaller cross-sections (MCSA = 4 m^2) while promoting channel lengthening. The slightly larger values of MCSA (8 m2) characterizing runs #4, #6, and #9 are likely due to the relatively uneven distribution of tidal channels shown in Figures 4d, f, and i. The drainage of the basin then requires, on average, a more intense water flux concentration within the channels and, hence, a larger cross-sectional area. The mean unchannelled length decreases exponentially with the total channel length (Figure 11b). The consistency of this power-law relationship is remarkably high ($R^2 = 0.973$) for all the simulated channel networks. In the absence of vegetation, the drainage efficiency exhibits a similar range of variation to changes in density and location of the initial perturbations (Figure 11c, runs #1 to #9, blue marks). Vegetation is found to produce longer channels with more branches and, eventually, more efficient drainage systems, especially for a flat bed (runs #1 to #3). Finally, as the initial bed slope increases (runs #2, #10, and #11), the drainage efficiency invariably decreases, regardless of the presence (red marks) or not (blue marks) of vegetation.

669 Remarkable is also the influence of tidal asymmetry (runs #12 and #13), as compared to
670 the reference case with a symmetrical tide (run #2). A flood-dominant forcing is characterized by
671 a lower drainageefficiency ($(lL_c)^{-1}$), whereas an ebb-dominant forcing is associated with a
672 higher drainage efficiency (Figure 11c, dark blue triangles). Indeed, when compared to run #2
673 (the hexagram marker in Figure 11b), both the flood- and ebb-dominant forcings generate longer
674 channels and shorter unchanneled lengths (dark blue triangles in Figure 11b). However, in the
675 ebb-dominant situation, the total channel length and the mean unchanneled length are smaller
676 than in the flood-dominant case, leading to larger value of $(lL_c)^{-1}$ and higher drainage
677 efficiency (Figure 11c).

678 Two key factors provide opposite effects on the channel network development observed
679 in the presence of a longitudinally sloping bed. On the one hand, the well-developed salt marshes
680 forming on sloping platforms promote channel elongation. On the other hand, channel growth is
681 restricted by a reduced tidal prism (Sgarabotto et al., 2021). The specific contributions of these
682 two factors on channel development are addressed in Figure 12.

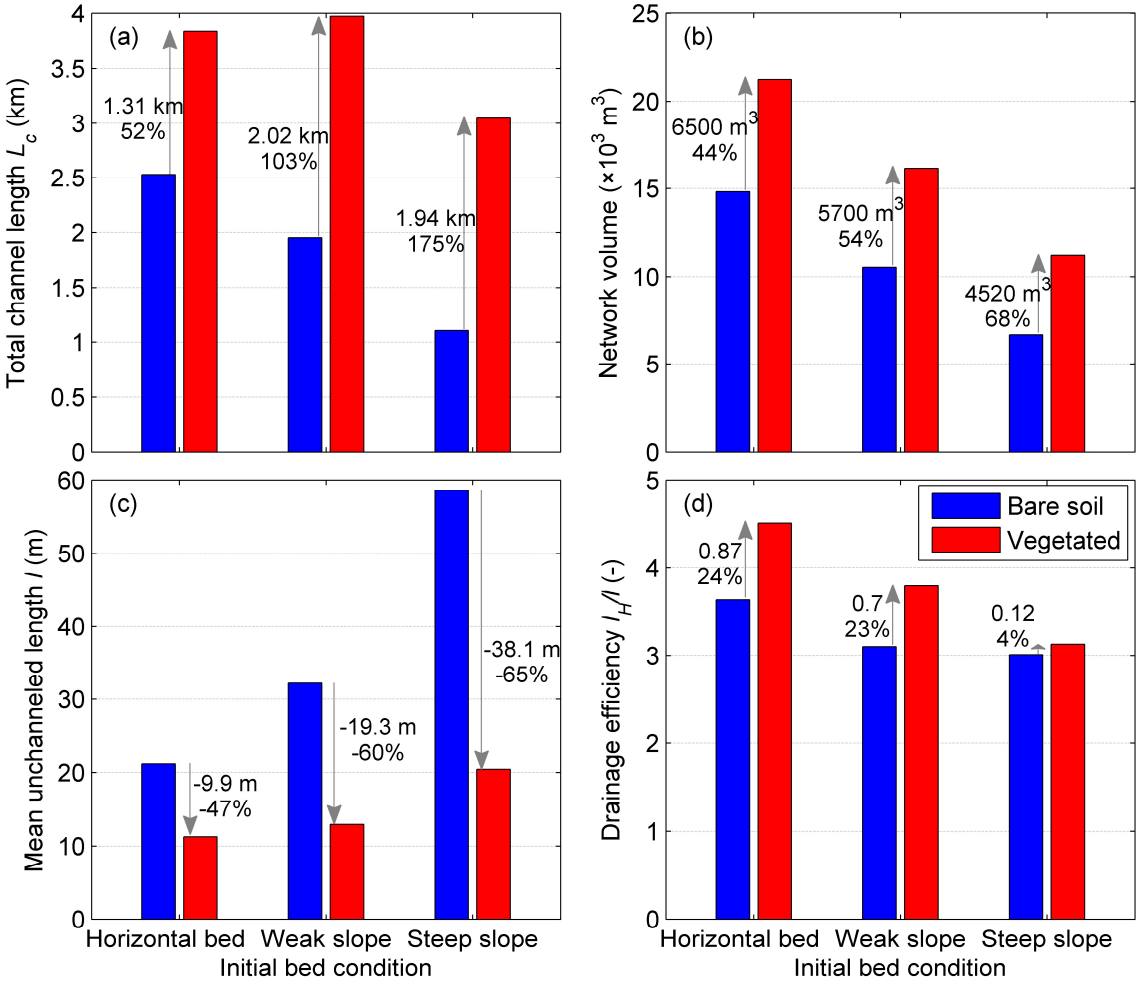

683

684 **Figure 12.** (**a**) The total channel length, (**b**) the channel network volume, (**c**) the mean
685 unchannelled length, and (**d**) the drainage efficiency at the end of simulations carried out for
686 different initial bed slopes either in the absence (blue bars) or in the presence (red bars) of

vegetation. The vegetation-induced changes (both absolute and relative values) are recorded in the panels.

For weakly sloping beds, vegetation leads to a longer total channel length as compared to the horizontal bed case (Figure 12a). However, a shorter total channel length is observed in the case of a steep bed slope, owing to the prevailing effect of the reduced tidal prism, which overcomes channel elongation induced by marsh growth. In any case, vegetation determines the formation of longer channels with respect to bare soil conditions. This elongation effect is particularly strong in the case of a steep bed slope, for which a 175% increase in channel length is observed.

Differently from the total channel length, the volume invariably decreases as the initial bed slope increases. Indeed, as the slope of the intertidal platform increases, the total channel volume reduces due to a smaller tidal prim. Moreover, the volume increase induced by vegetation remains almost constant (Figure 12b). This trend is explained by the fact that channel lengthening associated with vegetation growth (Figure 12a) is partly compensated by the formation of smaller cross-sections (Figure 11a).

The mean unchannelled length increases with the bed slope because of the shorter channels and, hence, the less dendritic networks induced by the smaller tidal prism (Figure 12c, blue bars). However, vegetation encroachment reduces this increase (Figure 12c, red bars) by incrementing channel branching.

The drainage efficiency is reduceed as the slope increases, while vegetation presence invariably enhances the drainage efficiency (Figure 12d). The decrease in mean unchannelled length observed when vegetation grows (Figure 12c), in fact, compensates by far channel elongation (Figure 12a), eventually leading to an increase in the product $(lL_c)^{-1}$. The growth in drainage efficiency induced by vegetation, however, becomes weaker as the longitudinal bed slope increases, even though the variations in both L_c and l get larger. This finding can be explained by considering the changes in the tidal prism. The smaller tidal prism, which characterizes a much steeper bathymetry, hampers the influence of vegetation on drainage efficiency (Figure 12d) and leads to smaller cross-sectional areas and, consequently, to a tidal network less efficient in draining the tidal basin during the ebb phase.

4.3 Comparisons with the field observations

The morphological trends and the channel-marsh interactions suggested by the present model results are here compared with the information arising from aerial photos collected in two tidal spots of Venice Lagoon, Italy, and Jiangsu Coast, China (Figure 13), and the reported channel-marsh co-evolutions in the Wester Scheldt Estuary, the Netherlands (Temmerman et al., 2007; Schwarz et al., 2018) and along the Yangtze Estuary, China (Schwarz et al., 2014).

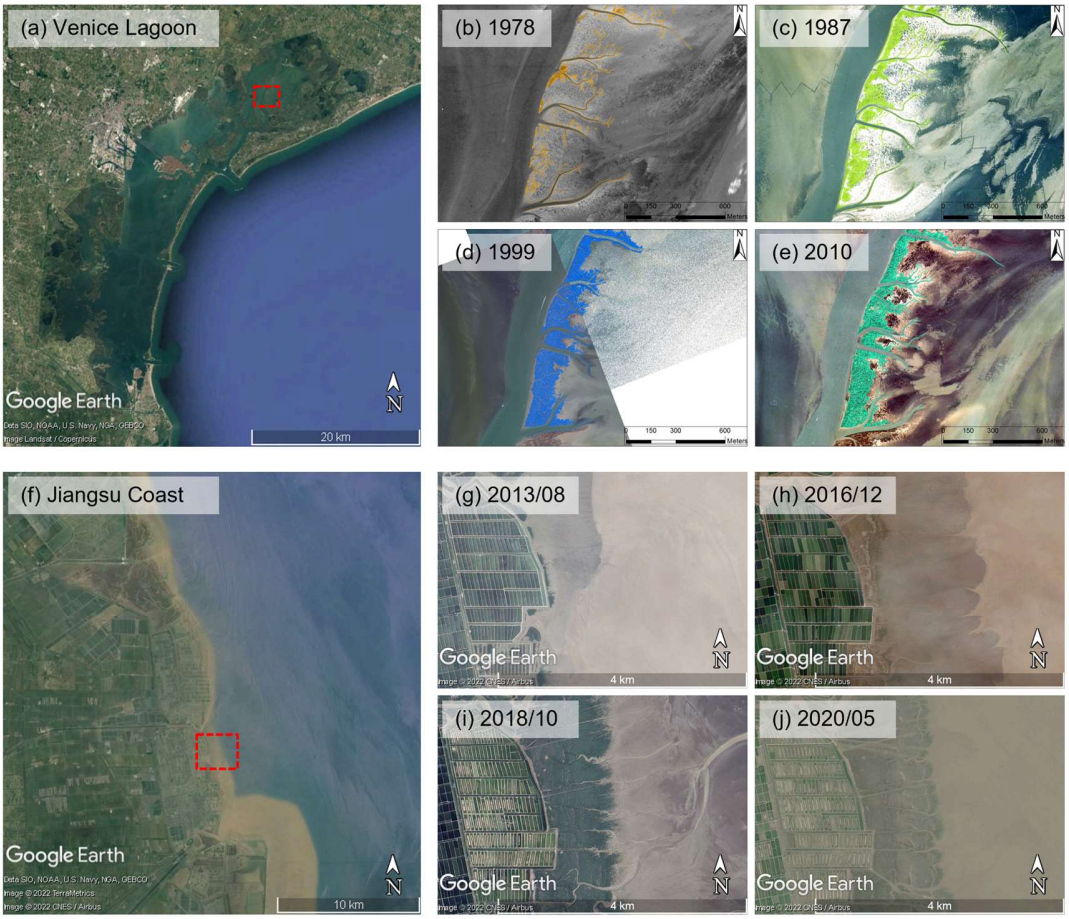

Figure 13. Two typical tidal spots in Venice Lagoon, Italy **(a)**, and along Jiangsu Coast, China **(f)**. Panels **(b-e)** and (**g-j**) show the co-evolution processes of channel-marsh systems in Venice Lagoon and along Jiangsu Coast, respectively.

In the case of the almost plane mudflats, as those flanking the Wester Scheldt Estuary and in Venice Lagoon (Figures 13a-e), vegetation encroachment progressively extends landwards, and the tidal channel system evolves accordingly (see Figure 1 in Schwarz et al., 2018), in qualitative accordance with the trends shown in Figure 5. This landward expansion is found to depend on the type of plants colonizing the Wester Scheldt mud flats (Schwarz et al., 2018). Fast colonizers species (e.g., Salicornia) are characterized by a high number of establishing seedlings which lead to homogenous vegetation patterns. Conversely, slow colonizers (e.g., Spartina) have a low number of establishing seedlings that can expand laterally, producing patchy vegetation patterns. In the presence of a fast-colonizing species, pre-existing channels are stabilized, and the fast colonizer consolidates the configuration of the tidal spot within a relatively short time. In contrast, slow colonizers promote the formation of new channels. In the present model, the slow- and fast-colonizing plant species is somewhat mimicked by increasing initial perturbation density (i.e., runs #1 to #3 with vegetation). However, in our simulations, no pre-existing channels are present, and channel formation occurs contemporarily with salt marsh evolution. Therefore, the evolution processes of the channel-marsh systems in runs #1 to #3 are similar to the situation with slow colonizers reported in Schwarz et al. (2018). Furthermore, the denser

742 vegetation patches are found to produce longer channels (Figure 11), with more branches and
743 high-order channels, but a smaller total cross-sectional area at the seaward boundary (Figure 10).

744 The present simulations suggest that vegetation grows best towards the landward end of
745 the domain (Figures 5h,l), even though this part has a lower elevation than the seaward part and,
746 hence, is characterized by a larger inundation stress. These controversial findings are possibly
747 related to the reduced complexity model used here for the vegetation. Indeed, the biomass is
748 simply related to the local tidal flat elevation (Figure 2d), a proxy of inundation frequency and
749 duration. At the end of the simulations, the lower seaward biomass density is due to the higher
750 elevation (e.g., Figures 5h,l), which exceed the optimal elevation for vegetation survival. In
751 reality, inundation stress also depends on micro-topography features, which can have effects on
752 sediment chemistry and plant performance similar in magnitude to those of overall tidal
753 elevation (Mossman et al., 2020). This is one of the reasons explaining the low vegetation
754 establishment success on poorly drained tidal flats (Crooks et al. 2002, Fivash et al. 2020,
755 Mossman et al. 2020).

756 The simulations carried out in the presence of a seaward sloping bed (Figure 7) exhibit a
757 trend consistent with the field observations available for the Chongming Island (Yangtze estuary,
758 China) and the Jiangsu Coast (Figures 13f-g), according to which vegetation first colonizes the
759 higher inner areas and then extends seawards (see Figure 7 in Schwarz et al., 2014). Moreover,
760 similarly to the model, more channel branches and more complex channel networks are observed
761 to form in the field after the salt marshes encroach the mudflats. As discussed in Section 3.3,
762 present results (Figure 7f) can also explain the formation of small isolated channels observed in
763 the field.

764 Overall, our simulations indicate that vegetation increases the drainage efficiency of tidal
765 channel networks, in agreement with other studies (e.g., Vandenbruwaene et al., 2013; Kearney
766 & Fagherazzi, 2016; Schwarz et al., 2022). In addition, once the vegetation has fully established
767 and the channels have been generated, a reduction of the tidal prism induced by continued
768 sediment accretion does not result in significant changes in channel features (e.g., Figures 7j and
769 7h), in accordance with the analysis carried out by Vandenbruwaene et al. (2013) on the basis of
770 a time series of aerial photographs and digital elevation models of the Western Scheldt Estuary at
771 Saeftinghe (The Netherlands). Indeed, this reduction is mainly due to a decrease of the volume of
772 water flowing over the vegetated areas, whereas the volume of water conveyed by channels does
773 not change too much.

774 The above reported comparisons suggest that, despite the intrinsic model limitations
775 (discussed in detail in the next section), insights of the present study may be used to support the
776 management of wetlands and the design of restoration projects in coastal areas. Because of
777 human activities and sea level rise, the global tidal flat area decreased by about 16% between
778 1984 and 2016 (Murray et al., 2019), and restoration efforts to protect degraded salt marsh
779 habitats are considerably increasing worldwide (Billah et al., 2022). Over the past few decades,
780 many intertidal areas have been planted with aquatic vegetation on bare soil to prevent land loss
781 and create new salt marshes (e.g., Craft et al., 2002; Chung, 2006; Pontee et al., 2016). This
782 study highlights the importance of evaluating the effectiveness of topographic manipulations and
783 different planting arrangements to be adopted in projects of marsh restoration and creation.

4.4 Model limitations

The present model has been found to produce meaningful evolutions of tidal channels and salt marshes in a schematic tidal basin. Nevertheless, some physical processes have been neglected or modelled in a simplified way, as described below. First, wind effects have been neglected, but they could play an important role in sediment resuspension and channel bank erosion, eventually affecting the growth of tidal networks (see, e.g., Mariotti & Fagherazzi, 2013; Ortiz et al. 2017). Second, bank erosion processes were not included in the modelling framework. This provides a simplified description of the evolution of channel cross sections, but underestimates channel widening (Bendoni et al., 2016; Leonardi et al., 2016; Zhao et al., 2021). Third, neglecting the changes in soil erodibility induced by vegetation roots may reduce the differences in channel patterns obtained in unvegetated and vegetated cases (De Battisti et al., 2019). On the other hand, vegetation encroachment on the intertidal platform can be better reproduced by considering the dispersion of vegetation seed and the lateral extension of vegetation patches due to rhizome growing (Temmerman et al., 2005; Silinski et al., 2016; Zhao et al., 2022). The present model lumps the effects of multi-species vegetation on the intertidal platform by using a specific biomass density function, which only depends on local bed elevation. However, vegetation biomass depends also on the inundation stress that is neglected here. The inundation stress may lead to smaller biomass production in the poorly-drained lower landward areas (Figures 5h,l) because of the lower oxygen level (Fivash et al., 2020; Mossman et al., 2020). Furthermore, the modelling approach neglects the dispersal and competitive dynamics between different vegetation species affecting the encroachment of the intertidal platforms (e.g., Finotello et al., 2022), as well as biotturbation by critters. Finally, in the present model, a constant mean sea level is assumed. However, relative sea level rise can limit vegetation growth, reduce the influence of salt marshes on channel evolution and prevent the system from reaching equilibrium conditions (e.g., Coco et al., 2013; Alizad et al., 2018; Oppenheimer et al., 2019; Geng et al., 2021). All these processes need to be accounted for in the model, at least conceptually, to characterize more robustly the critical factors controlling the formation of an efficient drainage system.

Besides the future improvement of the model, the morphological trends pointed out by this research should be evaluated in a broader range of tidal settings. We have, in fact, considered a tide-dominated basin adjacent to a relatively deep and large channel. As the system evolves, the level of the tidal platform close to the boundary channel progressively increases in elevation, acting as a barrier sheltering the tidal basin. Tidal channels then represent the preferential routes through which the tidal basin exchanges water with the sea, and the existence of a robust $P - A$ is definitely expected. On the other hand, along unsheltered coasts, a non-negligible part of the tidal prism is exchanged directly throughout the tidal flats when they are submerged. Therefore, the existence of a power-law relating the tidal prism to the tidal channel area needs to be carefully reconsidered in the case of the open coast environment.

5 Conclusions

The present study focused on the growth of tidal networks starting from an initial bathymetry, either horizontal or sloping, with a different density and distribution of relatively small perturbations. The sensitivity of equilibrium conditions to these initial conditions has been thoroughly discussed, considering or neglecting the vegetation encroachment.

827 Initial bathymetries obtained by changing the density (i.e., the number) of perturbations
828 mildly affect the morphology of tidal networks,which show similar values for channel length,
829 cross-sectional areas, and tidal prism between cases. On the other hand, by changing the
830 distribution of perturbations on the initial bathymetry, the structure and the size of tidal channel
831 networks exhibit more remarkable differences, and the corresponding $P - A$ relationship shows a
832 larger variations. This suggests that different distributions of initial perturbations may lead to
833 multiple equilibrium configurations, although the tidal system is subjected to the same forcings.

834 In vegetated scenarios, the initial perturbations can be regarded as micro-topography
835 features, which favor the formation of vegetation patches. Vegetation fosters the effects of the
836 initial bathymetry perturbations and increases the degree of complexity of the equilibrium tidal
837 channel networks. By trapping sediment coming from the sea, initially-denser vegetation patches
838 enhance the seaward salt marsh growth while reducing the amount of sediment delivered to the
839 inner basin area. Conversely, sparse initial bed perturbations promote a faster vegetation
840 encroachment in the landward portion of the basin.

841 In the presence of a initially seaward-sloping bed, the tidal prism is reduced with respect
842 to an initially horizontal bed, and tidal channels are shorter. When vegetation encroaches on the
843 intertidal platform, well-developed salt marshes first colonize the higher landward portions of the
844 tidal basin and then expand seaward. The flow concentration between vegetation patches always
845 favors channel formation and elongation, as well as the reduction of mean unchanneled length.

846 Asymmetry in the tidal forcing, created by overtides, is found to significantly affect
847 erosional processes and tidal channel evolution. In flood-dominated environments, erosional
848 processes are more evenly distributed across the tidal basin. Conversely, in ebb-dominated
849 environments, in-channel erosion prevails, favoring channel deepening and leading to smaller
850 width-depth ratios as compared to the flood-dominated scenario.

851 The channel network drainage efficiency, dependent on the unchanneled length, is
852 weakly influenced by the features of initial perturbations. The most significant effects on
853 drainage efficiency are provided by the initial bed slope and the presence of vegetation. For
854 situations with higher bed slopes, the reduction in tidal prism implies that a smaller volume of
855 water needs to be drained, which restricts the vegetation-induced promotion of drainage
856 efficiency and leads to less developed channel networks.

857 **Acknowledgments**

858 This research was supported by National Natural Science Foundation of China (Grant 51925905,
859 42206162, and 51879095), the Open Research Fund of State Key Laboratory of Estuarine and
860 Coastal Research (Grant SKLEC-KF202202), and the China Postdoctoral Science Foundation
861 (Grant 2022M711019). Special thanks are given to Prof. Tomas Van Oyen from Ghent
862 University and Prof. Mario Putti from the University of Padova for their support and suggestions
863 on this model.

864 **Data Availability Statement**

865 The modelling results used in the current study are available at
866 https://doi.org/10.5281/zenodo.7074400. The corresponding model scripts are available at
867 https://doi.org/10.5281/zenodo.7451878.

References

Alizad, K., Hagen, S. C., Medeiros, S. C., Bilskie, M. V., Morris, J. T., Balthis, L., & Buckel, C. A. (2018). Dynamic responses and implications to coastal wetlands and the surrounding regions under sea level rise. *PLoS One*, 13(10), e0205176. https://doi.org/10.1371/journal.pone.0205176

Bearman, J. A., Friedrichs, C. T., Jaffe, B. E., & Foxgrover, A. C. (2010). Spatial trends in tidal flat shape and associated environmental parameters in South San Francisco Bay. *Journal of Coastal Research*, 262, 342-349. http://doi.org/10.2112/08-1094.1

Beeftink, W. G. (1966). Vegetation and habitat of the salt marshes and beach plains in the south-western part of The Netherlands. *Wentia,* 15, 83-108

Belliard, J. P., Toffolon, M., Carniello, L., & D'Alpaos, A. (2015). An ecogeomorphic model of tidal channel initiation and elaboration in progressive marsh accretional contexts. *Journal of Geophysical Research: Earth Surface*, 120(6), 1040-1064. http://doi.org/10.1002/2015JF003445

Bendoni, M., Mel, R., Solari, L., Lanzoni, S., Francalanci, S., & Oumeraci, H. (2016). Insights into lateral marsh retreat mechanism through localized field measurements. *Water Resources Research*, 52(2), 1446-1464. https://doi.org/10.1002/2015WR017966

Billah, M. M., Bhuiyan, M. K. A., Islam, M. A., Das, J., & Hoque, A. T. M. (2022). Salt marsh restoration: an overview of techniques and success indicators. *Environmental Science and Pollution Research*, 29, 15347–15363. https://doi.org/10.1007/s11356-021-18305-5

Carniello, L., Defina, A., & D'Alpaos, L. (2009). Morphological evolution of the Venice lagoon: Evidence from the past and trend for the future. *Journal of Geophysical Research*, 114(F4) http://doi.org/10.1029/2008JF001157

Carniello, L., Defina, A., & D'Alpaos, L. (2012). Modeling sand-mud transport induced by tidal currents and wind waves in shallow microtidal basins: Application to the Venice Lagoon (Italy). *Estuarine Coastal and Shelf Science*, 102, 105-115. http://doi.org/10.1016/j.ecss.2012.03.016

Chung, C. H. (2006). Forty years of ecological engineering with Spartina plantations in China. *Ecological Engineering*, 27(1), 49-57. https://doi.org/10.1016/j.ecoleng.2005.09.012

Coco, G., & Murray, A. B. (2007). Patterns in the sand: From forcing templates to self-organization. *Geomorphology*, 91(3-4), 271-290. https://doi.org/10.1016/j.geomorph.2007.04.023

Coco, G., Zhou, Z., van Maanen, B., Olabarrieta, M., Tinoco, R., & Townend, I. (2013). Morphodynamics of tidal networks: Advances and challenges. *Marine Geology*, 346, 1-16. http://doi.org/10.1016/j.margeo.2013.08.005

Cox, R., Wadsworth, R. A., & Thomson, A. G. (2003). Long-term changes in salt marsh extent affected by channel deepening in a modified estuary. *Continental Shelf Research*, 23(17-19), 1833-1846. https://doi.org/10.1016/j.csr.2003.08.002

Craft, C., Broome, S., & Campbell, C. (2002). Fifteen Years of Vegetation and Soil Development after Brackish-Water Marsh Creation. *Restoration Ecology*, 10(2), 248–258. https://doi:10.1046/j.1526-100x.2002.01020.x

Crooks, S., Schutten, J., Sheern, G. D., Pye, K., & Davy, A. J. (2002). Drainage and elevation as factors in the restoration of salt marsh in Britain. *Restoration ecology*, 10(3), 591-602. https://doi.org/10.1046/j.1526-100X.2002.t01-1-02036.x

Da Lio, C., D'Alpaos, A., & Marani, M. (2013). The secret gardener: vegetation and the emergence of biogeomorphic patterns in tidal environments. *Philosophical Transactions of the Royal Society A: Mathematical, Physical and Engineering Sciences*, 371(2004), 20120367. https://doi.org/10.1098/rsta.2012.0367

D'Alpaos, A., Lanzoni, S., Marani, M., Fagherazzi, S., & Rinaldo, A. (2005). Tidal network ontogeny: Channel initiation and early development. *Journal of Geophysical Research-Earth Surface*, 110(F2), 351-394. http://doi.org/10.1029/2004JF000182

D'Alpaos, A., Lanzoni, S., Mudd, S. M., & Fagherazzi, S. (2006). Modeling the influence of hydroperiod and vegetation on the cross-sectional formation of tidal channels. *Estuarine, Coastal and Shelf Science*, 69(3-4), 311-324. https://doi.org/10.1016/j.ecss.2006.05.002

D'Alpaos, A., Lanzoni, S., Marani, M., & Rinaldo, A. (2007). Landscape evolution in tidal embayments: Modeling the interplay of erosion, sedimentation, and vegetation dynamics. *Journal of Geophysical Research*, 112(F1) http://doi.org/10.1029/2006JF000537

D'Alpaos, A., Lanzoni, S., Marani, M., & Rinaldo, A. (2009). On the O'Brien-Jarrett-Marchi law. *Rendiconti Lincei*, 20(3), 225-236. http://doi.org/10.1007/s12210-009-0052-x

D'Alpaos, A., Lanzoni, S., Marani, M., & Rinaldo, A. (2010). On the tidal prism - channel area relations. *Journal of Geophysical Research-Earth Surface*, 115(F01003), 1-13. http://doi.org/10.1029/2008JF001243

D'Alpaos, A., & Marani, M. (2016). Reading the signatures of biologic-geomorphic feedbacks in salt-marsh landscapes. *Advances in Water Resources*, 93(B), 265-275. http://doi.org/10.1016/j.advwatres.2015.09.004

De Battisti, D., Fowler, M. S., Jenkins, S. R., Skov, M. W., Rossi, M., Bouma, T. J., Neyland, P. J., & Griffin, J. N. (2019). Intraspecific root trait variability along environmental gradients affects salt marsh resistance to lateral erosion. *Frontiers in Ecology and Evolution*, 7:150. https://doi.org/10.3389/fevo.2019.00150

Defina, A. (2000). Two‐dimensional shallow flow equations for partially dry areas. *Water Resources Research*, 36(11), 3251-3264. http://doi.org/10.1029/2000WR900167

Defina, A., Carniello, L., Fagherazzi, S., & D'Alpaos, L. (2007). Self‐organization of shallow basins in tidal flats and salt marshes. *Journal of Geophysical Research: Earth Surface*, 112(F3). https://doi.org/10.1029/2006JF000550

Fagherazzi, S., & Furbish, D. J. (2001). On the shape and widening of salt marsh creeks. *Journal of Geophysical Research* 106 (C1), 991-1005. https://doi.org/10.1029/1999JC000115

Fagherazzi, S., & Sun, T. (2004). A stochastic model for the formation of channel networks in tidal marshes. *Geophysical Research Letters*, 31(21), 87-107. http://doi.org/10.1029/2004GL020965

Fagherazzi, S., Kirwan, M. L., Mudd, S. M., Guntenspergen, G. R., Temmerman, S., D'Alpaos, A., van de Koppel, J., Rybczyk, J. M., Reyes, E., Craft, C., & Clough, J. (2012). Numerical models of salt marsh evolution: ecological, geomorphic, and climatic factors. *Reviews Of Geophysics*, 50(RG1002) http://doi.org/10.1029/2011RG000359

Finotello, A., D'Alpaos, A., Marani, M., & Bertuzzo, E. (2022). A Minimalist Model of Salt-Marsh Vegetation Dynamics Driven by Species Competition and Dispersal. *Frontiers inMarine Science*, 9:866570. https://doi.org/10.3389/fmars.2022.866570

Fivash, G. S., Belzen, J. V., Temmink, R. J., Didderen, K., Lengkeek, W., Heide, T. V. D., & Bouma, T. J. (2020). Elevated micro-topography boosts growth rates in Salicornia procumbens by amplifying a tidally driven oxygen pump: implications for natural recruitment and restoration. *Annals of botany*, 125(2), 353-364. https://doi.org/10.1093/aob/mcz137

Friedrichs, C. T. (1995). Stability shear stress and equilibrium cross-sectional geometry of sheltered tidal channels. *Journal of Coastal Research*, 11(4), 1062-1074. https://doi.org/10.2307/4298411

Geng, L., Gong, Z., Lanzoni, S., & D Alpaos, A. (2018). A New Method for Automatic Definition of Tidal Creek Networks. *Journal of Coastal Research*, 85, 156-160. http://doi.org/10.2112/SI85-032.1

Geng, L., Gong, Z., Zhou, Z., Lanzoni, S., & D'Alpaos, A. (2020). Assessing the relative contributions of the flood tide and the ebb tide to tidal channel network dynamics. *Earth Surface Processes and Landforms*, 45(1), 237-250. http://doi.org/10.1002/esp.4727

Geng, L., D'Alpaos, A., Sgarabotto, A., Gong, Z., & Lanzoni, S. (2021). Intertwined Eco-Morphodynamic Evolution of Salt Marshes and Emerging Tidal Channel Networks. *Water Resources Research*, 57(11), 1-25. http://doi.org/https://doi.org/10.1029/2021WR030840

Geng, L. (2022). Data used in paper "The sensitivity of tidal channel systems under the influences of initial bed conditions, vegetation, and tidal asymmetry". [Data set]. Zenodo. https://doi.org/10.5281/zenodo.7074400

Geng, L. (2022). Numerical model for channel-marsh evolution used in paper "The Sensitivity of Tidal Channel Systems to Initial Bed Conditions, Vegetation, and Tidal Asymmetry". Zenodo. https://doi.org/10.5281/zenodo.7451878

Gibbs, R.J. (1985). Estuarine flocs e their size, settling velocity and density. *Journal of Geophysical Research-Oceans* 90 (NC2), 3249-3251. https://doi.org/10.1029/JC090iC02p03249

Gong, Z., Jin, C., Zhang, C., Zhou, Z., Zhang, Q., & Li, H. (2017). Temporal and spatial morphological variations along a cross-shore intertidal profile, Jiangsu, China. *Continental Shelf Research*, 144, 1-9. http://doi.org/10.1016/j.csr.2017.06.009

Hancock, G. R., Coulthard, T. J., & Lowry, J. B. C. (2016). Predicting uncertainty in sediment transport and landscape evolution - the influence of initial surface conditions. *Computers & Geosciences*, 90(May Pt.B), 117-130. http://doi.org/10.1016/j.cageo.2015.08.014

Hu, Z., Van Belzen, J., Van Der Wal, D., Balke, T., Wang, Z. B., Stive, M., & Bouma, T. J. (2015). Windows of opportunity for salt marsh vegetation establishment on bare tidal flats: The importance of temporal and spatial variability in hydrodynamic forcing. *Journal of Geophysical Research: Biogeosciences*, 120(7), 1450-1469. https://doi.org/10.1002/2014JG002870

Hughes, S. A. (2002). Equilibrium cross sectional area at tidal inlets. *Journal of Coastal Research*, 18(1), 160-174. West Palm Beach (Florida), ISSN 0749-0208.

Hughes, Z. J., FitzGerald, D. M., Wilson, C. A., Pennings, S. C., Więski, K., & Mahadevan, A. (2009). Rapid headward erosion of marsh creeks in response to relative sea level rise. *Geophysical Research Letters*, 36(3), 441-451. http://doi.org/10.1029/2008GL036000

Hume, T. M., & Herdendorf, C. E. (1993). On the use of empirical stability relationships for characterising estuaries. *Journal of Coastal Research*, 9(2), 413-422. Fort Lauderdale (Florida), ISNN 0749-0208.

Iwasaki, T., Shimizu, Y., & Kimura, I. (2013). Modelling of the initiation and development of tidal creek networks.

Proceedings of the ICE - Maritime Engineering, 166(2), 76-88. http://doi.org/10.1680/maen.2012.12

Jarrett, J. T. (1976). Tidal prism: Inlet area relationships. General investigation of tidal inlets, report 3. U.S. Army Coastal Engineering Research Center, Fort Belvoir, VA. U.S. Army Engineers Waterways Experiment Station, Vicksburg, MS, 32 pp

Kearney, W. S., & Fagherazzi, S. (2016). Salt marsh vegetation promotes efficient tidal channel networks. *Nature Communications*, 7(1), 1-7. http://doi.org/10.1038/ncomms12287

Kirwan, M. L., Guntenspergen, G. R., D'Alpaos, A., Morris, J. T., Mudd, S. M., & Temmerman, S. (2010). Limits on the adaptability of coastal marshes to rising sea level. *Geophysical Research Letters*, 37(23). https://doi.org/10.1029/2010GL045489

Kirwan, M. L., Guntenspergen, G. R., & Langley, J. A. (2014). Temperature sensitivity of organic-matter decay in tidal marshes. *Biogeosciences*, 11(17), 4801-4808. http://doi.org/10.5194/bg-11-4801-2014

Kleinhans, M. G., van Rosmalen, T. M., Roosendaal, C., & van der Vegt, M. (2014). Turning the tide: mutually evasive ebb- and flood-dominant channels and bars in an experimental estuary. *Advances in Geosciences*, 39, 21-26. http://doi.org/10.5194/adgeo-39-21-2014

Leonardi, N., Ganju, N. K., & Fagherazzi, S. (2016). A linear relationship between wave power and erosion determines salt-marsh resilience to violent storms and hurricanes. *Proceedings of the National Academy of Sciences*, 113(1), 64-68. http://doi.org/10.1073/pnas.1510095112

Li, R., Yu, Q., Wang, Y., Wang, Z. B., Gao, S., & Flemming, B. (2018). The relationship between inundation duration and Spartina alterniflora growth along the Jiangsu coast, China. *Estuarine, Coastal and Shelf Science*, 213, 305-313. http://doi.org/10.1016/j.ecss.2018.08.027

Lopes, C. L., Mendes, R., Caçador, I., & Dias, J. M. (2020). Assessing salt marsh extent and condition changes with 35 years of Landsat imagery: Tagus Estuary case study. *Remote Sensing of Environment*, 247, 111939. http://doi.org/10.1016/j.rse.2020.111939

Marani, M., Belluco, E., D'Alpaos, A., Defina, A., Lanzoni, S., & Rinaldo, A. (2003). On the drainage density of tidal networks. *Water Resources Research*, 39(2), 5029-5035. http://doi.org/10.1029/2001WR001051

Marani, M., Lanzoni, S., Silvestri, S., & Rinaldo, A. (2004). Tidal landforms, patterns of halophytic vegetation and the fate of the lagoon of Venice. *Journal Of Marine Systems*, 51(1-4), 191-210. http://doi.org/10.1016/j.jmarsys.2004.05.012

Marani, M., D'Alpaos, A., Lanzoni, S., Carniello, L., & Rinaldo, A. (2010). The importance of being coupled: Stable states and catastrophic shifts in tidal biomorphodynamics. *Journal of Geophysical Research*, 115(F4) http://doi.org/10.1029/2009JF001600

Marani, M., Da Lio, C., & D Alpaos, A. (2013). Vegetation engineers marsh morphology through multiple competing stable states. *Proceedings of the National Academy of Sciences*, 110(9), 3259-3263. http://doi.org/10.1073/pnas.1218327110

Marchi, E. (1990). Sulla stabilitá delle bocche lagunari a marea. *Rendiconti Lincei*, 1(2), 137-150. DOI: 10.1007/BF03001888

Mariotti, G., & Fagherazzi, S. (2013). Critical width of tidal flats triggers marsh collapse in the absence of sea-level rise. *Proceedings of the National Academy of Sciences*, 110(14), 5353-5356. http://doi.org/10.1073/pnas.1219600110

Meerman, C., Rottschäfer, V., & Schuttelaars, H. (2019). Influence of geometrical variations on morphodynamic equilibria in short tidal basins. *Ocean Dynamics*, 69(2), 221-238. http://doi.org/10.1007/s10236-018-1236-7

Mossman, H. L., Grant, A., & Davy, A. J. (2020). Manipulating saltmarsh microtopography modulates the effects of elevation on sediment redox potential and halophyte distribution. *Journal of Ecology*, 108(1), 94-106. https://doi.org/10.1111/1365-2745.13229

Mudd, S. M., Fagherazzi, S., Morris, J. T., Furbish, D. J., Fagherazzi, S., Marani, M., & Blum, L. K. (2004). Flow, sedimentation, and biomass production on a vegetated salt marsh in South Carolina: toward a predictive model of marsh morphologic and ecologic evolution. *Ecogeomorphology of Tidal Marshes*, 59, 165-188. http://doi.org/10.1029/CE059p0165

Murray, N. J., Phinn, S. R., DeWitt, M., Ferrari, R., Johnston, R., Lyons, M. B., et al. (2019). The global distribution and trajectory of tidal flats. *Nature*, 565(7738), 222-225. https://doi.org/10.1038/s41586-018-0805-8

O'Brien, M. P. (1969). Equilibrium flow areas of inlets on sandy coasts. *Journal of the Waterways and Harbors Division*, 95(1), 43-52. http://doi.org/10.10161/JWHEAU.0000622

Oppenheimer, M., Glavovic, B., Hinkel, J., van de Wal, R., Magnan, A. K., Abd-Elgawad, A., et al. (2019). Sea level rise and implications for low lying islands, coasts and communities. In H. Pörtner (Ed.), *IPCC special report on the ocean and cryosphere in a changing climate*. IPCC.

Ortiz, A. C., Roy, S., & Edmonds, D. A. (2017). Land loss by pond expansion on the mississippi river delta plain.

Geophysical Research Letters, 44(8). 3635–3642, https://doi:10.1002/2017GL073079.
Palmer, M. R., Nepf, H. M., Pettersson, T. J., & Ackerman, J. D. (2004). Observations of particle capture on a cylindrical collector: Implications for particle accumulation and removal in aquatic systems. *Limnology And Oceanography*, 49(1), 76-85. http://doi.org/10.4319/lo.2004.49.1.0076
Pennings, S. C., & Callaway, R. M. (1992). Salt marsh plant zonation: the relative importance of competition and physical factors. *Ecology*, 73(2), 681-690. http://doi.org/10.2307/1940774
Perron, J. T., & Fagherazzi, S. (2012). The legacy of initial conditions in landscape evolution. *Earth Surface Processes and Landforms*, 37(1), 52-63. http://doi.org/10.1002/esp.2205
Pritchard, D., Hogg, A. J., & Roberts, W. (2002). Morphological modelling of intertidal mudflats: the role of cross-shore tidal currents. *Continental Shelf Research*, 22(11-13), 1887-1895. http://doi.org/10.1016/S0278-4343(02)00044-4
Pontee, N., Narayan, S., Beck, M. W., & Hosking, A. H. (2016). Nature-based solutions: lessons from around the world. *Proceedings of the Institution of Civil Engineers - Maritime Engineering*, 169(1), 29–36. http://doi:10.1680/jmaen.15.00027
Rinaldo, A., Fagherazzi, S., Lanzoni, S., Marani, M., & Dietrich, W. E. (1999). Tidal networks 2. Watershed delineation and comparative network morphology. *Water Resources Research*, 35(12), 3905-3917. http://doi.org/10.1029/1999WR900237
Roberts, W., Le Hir, P., & Whitehouse, R. (2000). Investigation using simple mathematical models of the effect of tidal currents and waves on the profile shape of intertidal mudflats. *Continental Shelf Research*, 20(10-11), 1079-1097. http://doi.org/10.1016/S0278-4343(00)00013-3
Roner, M., Ghinassi, M., Finotello, A., Bertini, A., Combourieu-Nebout, N., Donnici, S., Gilli, A., Vannacci, M., Vigliotti, L., & Bellucci, L. G. (2021). Detecting the delayed signatures of changing sediment supply in salt-marsh landscapes: the case of the Venice lagoon (Italy). *Frontiers in Marine Science*, 1477. http://doi.org/10.3389/fmars.2021.742603
Schwarz, C., Ye, Q. H., van der Wal, D., Zhang, L. Q., Bouma, T., Ysebaert, T., & Herman, P. M. J. (2014). Impacts of salt marsh plants on tidal channel initiation and inheritance. *Journal of Geophysical Research: Earth Surface*, 119(2), 385-400. https://doi.org/10.1002/2013JF002900Schwarz, C., Gourgue, O., Van Belzen, J., Zhu, Z., Bouma, T. J., Van De Koppel, J., et al. (2018). Self-organization of a biogeomorphic landscape controlled by plant life-history traits. *Nature Geoscience*, 11(9), 672-677. https://doi.org/10.1038/s41561-018-0180-y
Schwarz, C., van Rees, F., Xie, D., Kleinhans, M. G., & van Maanen, B. (2022). Salt marshes create more extensive channel networks than mangroves. *Nature communications*, 13(1), 1-9. https://doi.org/10.1038/s41467-022-29654-1
Sgarabotto, A., D'Alpaos, A., & Lanzoni, S. (2021). Effects of Vegetation, Sediment Supply and Sea Level Rise on the Morphodynamic Evolution of Tidal Channels. *Water Resources Research*, 57(7), 1-24. http://doi.org/10.1029/2020WR028577
Strahler, A. N. (1952). Hypsometric (area-altitude) analysis of erosional topography. *Geological society of America bulletin*, 63(11), 1117-1142. https://doi.org/10.1130/0016-7606(1952)63[1117:HAAOET]2.0.CO;2
Silinski, A., Fransen, E., Bouma, T. J., Meire, P., & Temmerman, S. (2016). Unravelling the controls of lateral expansion and elevation change of pioneer tidal marshes. *Geomorphology*, 274, 106-115. http://doi.org/10.1016/j.geomorph.2016.09.006
Stefanon, L., Carniello, L., D Alpaos, A., & Lanzoni, S. (2010). Experimental analysis of tidal network growth and development. *Continental Shelf Research*, 30(8), 950-962. http://doi.org/10.1016/j.csr.2009.08.018
Tambroni, N., & Seminara, G. (2006). Are inlets responsible for the morphological degradation of Venice Lagoon? *Journal of Geophysical Research: Earth Surface*, 111(F3). http://doi.org/10.1029/2005JF000334
Tambroni, N., & Seminara, G. (2009). On the theoretical basis of O'Brien−Jarrett−Marchi law for tidal inlets and tidal channels. In: Vionnet, M., Garcia, H., Latrubesse, E. M., Perillo, G. M. E. (eds), Proceedings of the 6th IAHR symposium on river, coastal and estuarine morphodynamics, 21-25 September 2009, Santa Fe, Argentina, C. A. 1, pp. 329-335, Taylor and Francis/Balkema.
Temmerman, S., Bouma, T. J., Govers, G., Wang, Z. B., De Vries, M. B., & Herman, P. M. J. (2005). Impact of vegetation on flow routing and sedimentation patterns: Three-dimensional modeling for a tidal marsh. *Journal of Geophysical Research: Earth Surface*, 110(F4). http://doi.org/10.1029/2005JF000301
Temmerman, S., Bouma, T. J., van de Koppel, J., van der Wal, D., De Vries, M. B., & Herman, P. M. J. (2007). Vegetation causes channel erosion in a tidal landscape. *Geology*, 35(7), 631. http://doi.org/10.1130/G23502A.1
Temmerman, S., Moonen, P., Schoelynck, J., Govers, G., & Bouma, T. J. (2012). Impact of vegetation die-off on spatial flow patterns over a tidal marsh. *Geophysical Research Letters*, 39(3). http://doi.org/10.1029/2011GL050502

Ter Brake, M. C., & Schuttelaars, H. M. (2010). Modeling equilibrium bed profiles of short tidal embayments. *Ocean Dynamics*, 60(2), 183-204. http://doi.org/10.1007/s10236-009-0232-3

Toffolon, M., & Lanzoni, S. (2010). Morphological equilibrium of short channels dissecting the tidal flats of coastal lagoons. *Journal of Geophysical Research-Earth Surface*, 115(F04036), 701-719. http://doi.org/10.1029/2010JF001673

Tognin, D., D'Alpaos, A., Marani, M., & Carniello, L. (2021). Marsh resilience to sea-level rise reduced by storm-surge barriers in the Venice Lagoon. *Nature Geoscience*, 14(12), 906-911. https://doi.org/10.1038/s41561-021-00853-7

Tommasini, L., Carniello, L., Ghinassi, M., Roner, M., & D'Alpaos, A. (2019). Changes in the wind−wave field and related salt−marsh lateral erosion: inferences from the evolution of the Venice Lagoon in the last four centuries. *Earth Surface Processes and Landforms*, 44(8), 1633-1646. http://doi.org/10.1002/esp.4599

van der Wegen, M., Wang, Z. B., Savenije, H. H. G., & Roelvink, J. A. (2008). Long-term morphodynamic evolution and energy dissipation in a coastal plain, tidal embayment. *Journal of Geophysical Research-Earth Surface*, 113(F03001F3), 337-344. http://doi.org/10.1029/2007JF000898

van der Wegen, M., Dastgheib, A., & Roelvink, J. A. (2010). Morphodynamic modeling of tidal channel evolution in comparison to empirical PA relationship. *Coastal Engineering*, 57(9), 827-837. http://doi.org/10.1016/j.coastaleng.2010.04.003

van Oyen, T., Carniello, L., D'Alpaos, A., Temmerman, S., Troch, P., & Lanzoni, S. (2014). An approximate solution to the flow field on vegetated intertidal platforms: Applicability and limitations. *Journal of Geophysical Research: Earth Surface*, 119(8), 1682-1703. http://doi.org/10.1002/2013JF003064

Vandenbruwaene, W., Temmerman, S., Bouma, T. J., Klaassen, P. C., de Vries, M. B., Callaghan, D. P., van Steeg, P., Dekker, F., van Duren, L. A., Martini, E., Balke, T., Biermans, G., Schoelynck, J., & Meire, P. (2011). Flow interaction with dynamic vegetation patches: Implications for biogeomorphic evolution of a tidal landscape. *Journal of Geophysical Research: Earth Surface*, 116(F1). http://doi.org/10.1029/2010JF001788

Vandenbruwaene, W., Bouma, T. J., Meire, P., & Temmerman, S. (2013). Bio‐geomorphic effects on tidal channel evolution: impact of vegetation establishment and tidal prism change. *Earth Surface Processes and Landforms*, 38(2), 122-132. https://doi.org/10.1002/esp.3265

Vlaswinkel, B. M., & Cantelli, A. (2011). Geometric characteristics and evolution of a tidal channel network in experimental setting. *Earth Surface Processes and Landforms*, 36(6), 739-752. http://doi.org/10.1002/esp.2099

Xu, F., Coco, G., Zhou, Z., Tao, J., & Zhang, C. (2017). A numerical study of equilibrium states in tidal network morphodynamics. *Ocean Dynamics*, 67(12), 1593-1607. http://doi.org/10.1007/s10236-017-1101-0

Yapp, R. H., Johns, D., & Jones, O. T. (1916). The salt marshes of the Dovey Estuary. Part I. Introductory. *Journal of Ecology*, 4, 27-42.

Yapp, R. H., Johns, D., & Jones, O. T. (1917). The salt marshes of the Dovey Estuary. Part II. The salt marshes. *Journal of Ecology*, 5, 65-103.

Zhang, R. S., Shen, Y. M., Lu, L. Y., Yan, S. G., Wang, Y. H., Li, J. L., & Zhang, Z. L. (2004). Formation of Spartina alterniflora salt marshes on the coast of Jiangsu Province, China. *Ecological Engineering*, 23(2), 95-105. http://doi.org/10.1016/j.ecoleng.2004.07.007

Zhang, Y., Zhou, Z., Geng, L., Coco, G., Tao, J., & Zhang, C. (2018). Simulating the formation of tidal channels along an open-coast tidal flat: the effects of initial perturbation. *Coastal Engineering Proceedings, 1*(36), papers.84. http://doi.org/10.9753/icce.v36.papers84

Zhao, K., Lanzoni, S., Gong, Z., & Coco, G. (2021). A Numerical Model of Bank Collapse and River Meandering. *Geophysical Research Letters*, 48(12) http://doi.org/10.1029/2021GL093516

Zhao, K., Coco, G., Gong, Z., Darby, S. E., Lanzoni, S., Xu, F., Zhang, K., & Townend, I. (2022). A review on bank retreat: mechanisms, observations, and modeling. *Reviews Of Geophysics*, 60(2), e2021R-e2761R. http://doi.org/10.1029/2021RG000761

Zhou, Z., Olabarrieta, M., Stefanon, L., D'Alpaos, A., Carniello, L., & Coco, G. (2014). A comparative study of physical and numerical modeling of tidal network ontogeny. *Journal of Geophysical Research: Earth Surface*, 119(4), 892-912. http://doi.org/10.1002/2014JF003092

Zhou, Z., Stefanon, L., Olabarrieta, M., D'Alpaos, A., Carniello, L., & Coco, G. (2014). Analysis of the drainage density of experimental and modelled tidal networks. *Earth Surface Dynamics*, 2(1), 105-116. http://doi.org/10.5194/esurf-2-105-2014

Zhou, Z., Coco, G., Townend, I., Olabarrieta, M., van Der Wegen, M., Gong, Z., D Alpaos, A., Gao, S., Jaffe, B. E., & Gelfenbaum, G. (2017). Is "morphodynamic equilibrium" an oxymoron? *Earth-Science Reviews*, 165, 257-267. https://doi.org/10.1016/j.earscirev.2016.12.002

1146